Characterization and Rationalization of Microstructural Evolution in GRCop-84 Processed by Laser-Powder Bed Fusion (L-PBF)



ROBERT P. MINNECI, MICHAEL P. HAINES, PAUL R. GRADL, DAVID L. ELLIS, ERIC A. LASS, JEFFREY R. BUNN, HAHN CHOO, ZACHARY C. JONES, SUDARSANAM S. BABU, and CLAUDIA J. RAWN

Prismatic geometries of GRCop-84 [Cu-8Cr-4Nb (at. pct)] were built with laser-powder bed fusion (L-PBF) process. The samples were sectioned parallel or perpendicular to the build direction and characterized in the as-built and after post-processing with a hot-isostatically pressing (HIP) treatment. The microstructure and phase evolutions were evaluated with optical microscopy, scanning electron microscopy (SEM), electron backscattered diffraction (EBSD), and high-temperature X-ray diffraction (HTXRD) up to 1223 K. The samples in the as-built conditions exhibited predominantly columnar epitaxial and misoriented Cu-FCC grains. The microstructure evolutions are discussed based on locations within the overall build geometry, the dynamics of small melt pool shape and sectioning effects. The above grain structure did not change significantly during post-process HIP treatment. The stability of this FCC grain structure is attributed to the formation of primary stable Cr₂Nb (Laves phase) during L-PBF, even before the emergence of FCC grains from liquid. The stability of Cr₂Nb in both as-built and HIPed samples were evaluated using high-temperature X-ray diffraction measurements and compared with that of gas-atomized powder. The significance of these results is discussed with reference to aerospace applications.

https://doi.org/10.1007/s11661-024-07315-w © The Minerals, Metals & Materials Society and ASM International 2024

I. INTRODUCTION

THE alloy GRCop-84, with a composition of Cu-8Cr-4Nb (at. pct), is a leading candidate for structural high-heat-flux applications requiring high thermal conductivity, retention of mechanical strength at high

ROBERT P. MINNECI. ERIC A. LASS. HAHN CHOO. CLAUDIA J. RAWN are with the Department of Materials Science and Engineering, University of Tennessee, Knoxville, TN 37996-2100. Contact e-mail: e-mail: crawn@utk.edu MICHAEL P. HAINES is with the Mechanical, Aerospace, Biomedical Engineering Department, University of Tennessee, Knoxville, TN 37996-2100. PAUL R. GRADL and ZACHARY C. JONES are with the NASA Marshall Space Flight Center, Huntsville, AL 35808. DAVID L. ELLIS is with the NASA Glenn Research Center, Cleveland, OH 44135. JEFFREY R. BUNN is with the Neutron Scattering Division, Oak Ridge National Laboratory, Oak Ridge, Tennessee 37831-6475. SUDARSANAM S. BABU is with the Department of Materials Science and Engineering, University of Tennessee and with the Mechanical, Aerospace, Biomedical Engineering Department, University of Tennessee and also with the Manufacturing Demonstration Facility, Manufacturing Sciences Division Oak Ridge National Laboratory, Oak Ridge, Tennessee 37831-6475.

Manuscript submitted August 17, 2023; accepted January 7, 2024. Article published online February 28, 2024

temperatures, and resistance to fatigue and creep. [1,2] Successful deployment of GRCop-84 components with complex geometries, for distributing coolants, through emerging additive manufacturing (AM) processes is critical. [3–5] Customized geometries and longer lifetimes result in increased reusability of components which has significant cost benefits, and allows for higher useable temperature ranges that improve safety margins and fuel efficiency in aerospace applications. [2] Currently, the best candidate copper alloys for aerospace applications needing both good mechanical properties and thermal management include NARloy-Z, AMZIRC, GlidCop, Cu-Cr, Cu-Cr-Zr, and GRCop alloys (both GRCop-84 and GRCop-42). [6] The typical alloy and design strategies focus on using a Cu-FCC matrix with minimal alloying element concentration, usually less than 1 wt pct, allowing for Cu's high thermal conductivity to be preserved. Higher thermal conductivity results in better cooling efficiency; however, the compromise between long- or short-term thermal and mechanical creep and fatigue issues must be addressed.

GRCop-84 alloy contains roughly 6.5 wt pct Cr and 5.7 wt pct Nb which is unusually high compared to the other competing alloys. The high alloying content limits GRCop-84's thermal conductivity. As a result, the

competing alloys generally outperform GRCop-84 below 773 K.^[7] Nevertheless, the precipitation of stable Cr₂Nb (Laves phase with C15 crystal structure) leads to a stable microstructure at high temperatures up to 1073 K.

GRCop alloys are usually produced by rapid solidification through gas atomization followed by powder metallurgy routes. [6] Cr and Nb have low solubility in Cu, in both liquid and in the FCC solid, and therefore, preferentially react with each other to form Cr₂Nb. Typical GRCop microstructures consist of a largely Cu-FCC matrix grains and micron-scale Cr₂Nb precipitates. Since the Cr₂Nb dissolution temperature in the liquid is > 1849 K, rapid solidification is necessary to limit the Cr₂Nb growth even in liquid. [8,9] Rapid solidification also reduces the size of the Cu matrix grains. A slight excess of Cr is added in alloying to prevent Nb precipitates from forming and potentially causing embrittlement under an H-rich atmosphere. [10]

A variety of consolidation methods have been applied to GRCop-84, including extrusion, metal spinning, vacuum plasma spraying, and tube drawing, but these methods are not capable of manufacturing complex geometries necessary for emerging aerospace applications. [11] In contrast, additive manufacturing (AM) allows for near net-shaped production of complex geometries with internal geometries that are unachievable by traditional methods and provides a significant improvement to performance. [12] Recent efforts with AM GRCop-84 through laser-powder bed fusion (L-PBF) has provided evidence that AM is an ideal consolidation method for GRCop-84. [2,4,13,14]

Haves et al., showed that the edges of the laser weldments have a high density of Cr₂Nb precipitates.^[15] This observation demonstrates a bias in the precipitate distribution caused by the laser motion, and the matrix grains may be affected by regions with different precipitate densities. GRCop gas-atomized powders usually have a bimodal distribution of Cr₂Nb particles with primary precipitate particles on the order of 1 μ m that form during solidification, and secondary precipitate particles on the order of 10-100 nm that could precipitate out of solution during cooling.[10] During consolidation with L-PBF, the melt pool temperature exceeds the melting temperature of Cr₂Nb (~2006 K), likely affecting the precipitate particle distribution. The Cr₂Nb precipitates within the gas-atomized powders ranged 0.2 to 1.6 μm, while the Cr₂Nb precipitates in the L-PBF builds were $< 0.2 \mu m$. This result supports that the Cr₂Nb particles dissolved in liquid Cu and re-precipitated. These small precipitates (~100 nm size), were found to be stable even at 1273 K. Although the overall cooling rate of the powder particles during gas atomization and L-PBF may be in the order of 10⁵ to 10⁶ K/s, the formation of solidification shell around the larger powder particles may reduce the cooling rate internally and promote particle coarsening.

Typical post-processing of these alloys often includes hot isostatic pressing (HIP) to relieve thermal residual stresses and reduce process-induced porosities and defects resulting from a lack of fusion. Demeneghi et al., [17] showed substantial reduction in porosity after HIP treatment and that the sensitivity of microstructure evolution during

L-PBF processing was correlated to the wall thickness in the design, which provides evidence of complex grain shape, size, and FCC crystallographic texture spanning a wide range of orientations with reference to build geometry, in both as-deposited and HIPed conditions. The as-deposited regions of L-PBF materials are expected to have a large amount of stored energy from the repetitive cyclic thermo-mechanical deformation potentially leading to large changes in the grain structure during HIP processing above the recrystallization temperature range from 473 to 873 K. Surprisingly, Demeneghi et al. [17] indicated a stable grain structure in L-PBF builds and no significant changes after the HIP post-processing.

The mobility of grain boundaries during heat treatment is controlled by the initial microstructure created by the L-PBF process, e.g., misorientation across the boundaries and the presence of precipitates along the boundaries.^[18] The microstructural evolution during fusion-based additive manufacturing techniques (i.e., DED, E-PBF, and L-PBF) is similar to welding, except for complex boundary conditions. Classical welding solidification parameters can be used to understand the final microstructure in L-PBF builds. The two parameters commonly used to understand solidification are the temperature gradient, G, measured in K/m, and the solid/liquid interface growth rate, referred to as solidification rate or interface velocity, R, measured in m/s. Both G and R parameters are functions of position and time within the melt pool. The product, G*R, is the cooling rate in K/s, which influences the scale of the resulting grains while G/R can be used to manipulate the solidification microstructure morphology. [19–21] At the fusion line, the solidification rate, R, will be roughly zero as the previous layer has solidified and will be unaffected by the laser pass, resulting in a G/R ratio that is effectively infinite and results in a planar-dominated grain structure at the bottom of the melt pool. [22] The interface then transitions sequentially into a cellular, columnar dendritic, and equiaxed dendritic interface as G/R decreases. The exact magnitude of G/R necessary to transition from one type of interfacial morphology to the next is dependent upon a variety of factors including undercooling, solute diffusion, slope of the liquidus curve, nominal alloy composition, and equilibrium partitioning ratio. [23] Typical L-PBF microstructures have either columnar or mixed columnar and equiaxed grain structures. [21,24] By manipulating the G and R, spatially and temporally, it is possible to arrive at site-specific grain structures. [22,25]

In this paper, we seek to combine the experimental characterization tools of room- and high-temperature XRD, SEM, and EBSD, along with thermodynamic modeling to explore the unique microstructure evolution in GRCop-84 that results in a stable microstructure during post-processing.

II. MATERIALS AND METHODS

A. Materials and Processing Conditions

L-PBF GRCop-84 samples were fabricated at NASA Marshall Space Flight Center (MSFC) on a Concept Laser M2 using a 400 W Nd:YAG 1064 nm laser with a

measured actual spot size of ~ 52 micrometers at the bed level, laser power of 178 W, scan speed of 585 mm/s, hatch spacing of 0.105 mm, layer thickness of 0.030 mm, and a chess scan pattern. The above parameters result in an energy density of about 97 J/mm³. As part of the L-PBF process, a layer of Inconel 625 was printed onto the stainless-steel build plate using a separate additive system, the build plate was cleaned of powder, and then the GRCop-84 build was initiated on top of the Inconel layer. This specific process was previously developed because GRCop-84 does not wet or adhere well to the stainless-steel build plate. [5] The Inconel 625 remains behind on the build plate when the part is wire electrical discharge machined (EDM) from the build plate. Parts were either in the form of 10 mm cubes or 10 x 10 mm² pillars with heights of 22 and 40 mm. A subset of parts was subsequently HIPed in an argon atmosphere above the recrystallization temperature. Details of the HIP parameters are unavailable for disclosure. Both the as-built and HIPed cubes and pillars are shown in Figure 1(a). The HIPed samples were significantly darker compared to the as-built samples; however, this discoloration was readily removed with polishing, suggesting that a thin oxide layer formed on the surface, despite the argon atmosphere. The presence of a small amount of oxygen is difficult to avoid and could be introduced during several different stages of the post-processing heat treatment. On a macro-scale, there were no observable external abnormalities or defects. The sides of the samples were relatively smooth, and the chess scan strategy used to produce the samples was observable on the top surface as shown in Figure 1(b). Figures 1(c), (d) are schematics that illustrate how the laser scan path changed between layers and overlapping regions. Samples for various characterization experiments used in this study were sectioned from both as-built and HIPed pillars with a laboratory saw either parallel (XZ) or perpendicular (XY)

to the build direction from a variety of locations. No etchants were needed or used for microscopy.

Chemical analysis was conducted at NASA Glenn Research Center (GRC) on as-built samples to estimate the elemental fractions. The measured data are compared to the target compositions in Table I. At 10 ppm, the Fe content was significantly lower than the specified maximum of 50 ppm, the O could not be reliably detected, and some additional impurities were present totaling to ~ 14 ppm.

B. Microstructure Characterization

Sectioned samples were mounted and ground with 4000-grit SiC paper on an auto-polisher then polished to $0.5 \mu m$ with a diamond suspension and finished with a vibratory polisher and colloidal silica (Syton HT-50). Electron backscattered images were collected with a Phenom ProX scanning electron microscope (SEM) at 15 kV, and electron backscatter diffraction (EBSD) mapping was conducted with a TESCAN MIRA 3 instrument. The EBSD maps were collected at 800x magnification with a step size of 250 nm, sample incline of 70 deg to the incident beam, working distance of 20-25 mm, beam intensity of 20 kV, current of 2.3 nA, and spot size of 26 nm. The resulting data correspond to Cu-FCC orientation maps, the Cr₂Nb precipitates were unindexable. The isolation of the pixels was achieved with ImageJ software. The EBSD mapping data were processed using the MTEX toolbox in MATLAB. [26]

C. Thermodynamic Calculations

Computational thermodynamic calculations were carried out using ThermoCalc® software coupled with the Copper database. Approximate melt pool characteristics pertaining to shape and temperature distribution were

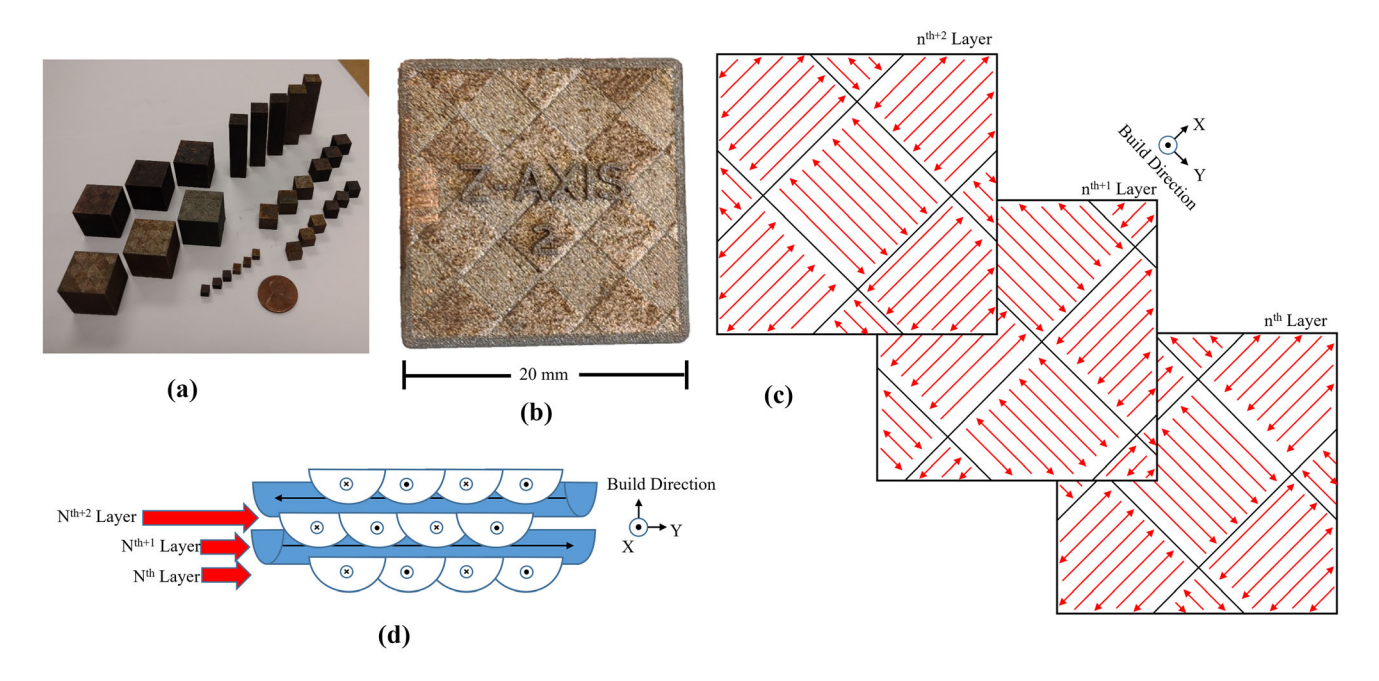


Fig. 1—L-PBF GRCop-84 (a) as-built and HIPed cubes and pillars (b) top of a cube; (c) schematic illustration (not to scale) of the idealized laser scan path on three consecutive XY planes (d) schematic illustration (not to scale) showing the layers and melt pool overlap.

Table I. Measured and Target Compositions of GRCop-84 As-Built Samples

Element	Cu	Cr (Wt Pct)	Nb (Wt Pct)	Fe (ppm)	O (ppm)	Other (ppm)
Measured Target	bal. bal.	6.47 6.2 - 6.8	5.78 5.4 - 6.0	10 < 50		< 14 < 100

calculated using analytical heat transfer equations^[27,28] for welding based on classical work by Rosenthal^[29,30] and later modified by Grong.^[31] The details of CET calculations can be found in Haines et al.^[32]

D. X-Ray Diffraction

Cross-sectional samples, 10 x 10 mm², were lightly polished by hand to a consistent surface to remove any artifacts. X-ray diffraction data were collected using a Malvern PANalytical Empyrean X-ray diffractometer with Cu radiation and a PIXcel detector. High-temperature X-ray diffraction (HTXRD) data were collected using an Anton Paar HTK1200N environmental chamber. The temperature was ramped from room temperature to 1223 K at a ramp rate of 3 K/min collecting a dataset every three minutes. Additional data were collected on the gas-atomized powder; however, the maximum temperature was set to 1123 K to avoid melting (the melting temperature of pure Cu is 1358 K). During ramping, data were collected over a range of 35 to 53 deg 2θ containing the Cu (111) and (200), the C15 Laves Cr_2Nb (220), (311), and (222), and additional reflections from possible oxides when detected. Scans from 30 to 100 deg 2θ were collected at room temperature prior to heating, at the maximum temperature after a dwell of approximately 10 minutes, and after cooling back to room temperature. For the as-built and HIPed samples, despite data being collected under vacuum, the surfaces of the samples showed a dark discoloration from oxidation. The surfaces were cleaned, post-heating, with a high grit grinding pad and water, and additional room temperature data were collected. Data were analyzed with the Rietveld technique using the General Structure Analysis System (GSAS II), [33–35] software package. Crystallographic information files (CIF), obtained from the Inorganic Crystal Structure Database (ICSD) database, were used for the initial models of the FCC Cu, BCC Cr, and cubic C15 Laves Cr₂Nb (Inorganic Crystal Structures Database (ICSD) Crystallographic Information File (CIF) numbers 43493, 64711, and 150658, respectively).

III. RESULTS & DISCUSSION

A. Microstructures of As-Built and HIPed Samples

1. As-built microstructure

SEM images, from the as-built samples, are shown in Figure 2 with high-contrast imaging allowing for delineation of Cu matrix grains and precipitates. Matrix

grains, precipitates, and defects are visible in both the XY and XZ sections. A bimodal distribution, long columnar grains surrounding regions of smaller equiaxed grains, of the matrix grains are seen for the XY section in Figure 2(a) and the XZ section in Figure 2(b). Three distinct precipitate distributions, labeled on Figure 2(c), were identified as following: (I) fine Cr₂Nb ($<0.25 \mu m$); (II) agglomerates of the fine type I Cr₂Nb particles; and (III) larger Nb-rich spherical particles. Due to the similarity in size, the type II and III particles can be difficult to distinguish, but the type III Nb-rich particles are brighter in the backscattered images and slightly larger than the type II particles. The particles are present at both grain boundaries and within grains. Particle reinforcement from Orowan strengthening is expected to provide a significant portion of strengthening to the alloy; further discussion of the strengthening features in GRCop-84 can be found in Minneci et al. [11] Within this microstructure, the primary Orowan contributions should be the Cr₂Nb particles on the grain boundaries which is mostly accounted for by the type I and II particles. The type III particles are likely too soft and too large to aid Orowan strengthening and do not exhibit an inclination towards grain boundaries. Voids or build defects (appearing with dark contrast) were observed across the as-built samples. Figures 2(a), (b) shows circular pores, possibly resulting from dissolved or trapped gas bubbles, and Figure 2(d), a low magnification image, shows lines of lack of fusion defects and evidence of particles trapped within voids. Figure 2(e) shows a SEM micrograph and a corresponding energy-dispersive X-ray spectroscopy (EDS) line scan through two brightly imaging type III particles. Across the grains, only minor compositional changes are detected, however, the EDS line scans indicate that the bright areas are particles rich in both Cr and Nb and are identified as Cr₂Nb. Converting from wt pct to at. pct, there are almost equal amounts of Nb and Cr; however, the phase diagram only shows one intermediate compound Cr₂Nb, with high- and low-temperature forms, and about 9 at. pct solid solution. [36] Additionally, the EDS line scans may not be able to provide a quantitative measure of the precipitate composition due to overlap of signals from Cu matrix.

2. HIPed microstructure

Following HIP treatment, the bimodal distribution of Cu matrix grains from the as-built condition was retained and is shown in Figures 3(a), (b) for the XY and XZ sections, respectively. In addition to the bright type I, II, and III particles, there are numerous small

back particles denoted as type IV in Figure 3(c). Figure 3(d) includes images representative from both XY and XZ sections revealing annealing twins (T) and recrystallized (Rx) regions. These are expected since the HIP temperature was above the recrystallization and annealing temperatures typical for GRCop-84 alloys. Type I, II, and III particles were not observed within the twinned grains or recrystallization regions; however,

there were some limited type IV particles observed in both. The boundaries between both annealing twins and recrystallized regions with their surrounding matrix grains show a high density of type I and II particles. Figure 3(e) shows a SEM micrograph and an associated EDS line scan across a darkly imaging particle, indicating that these are Cr particles.

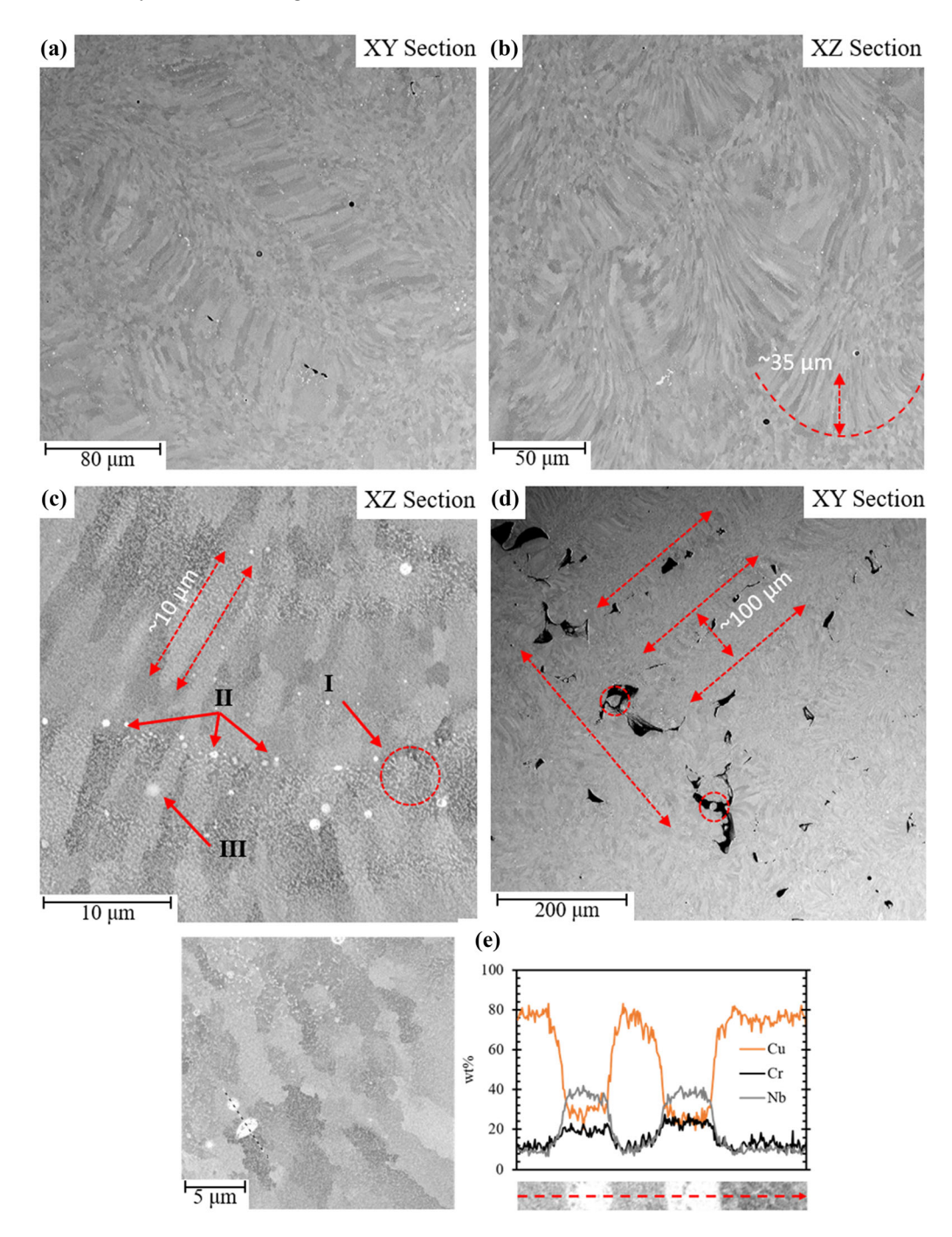


Fig. 2—SEM images for the as-built GRCop-84 samples (a) XY section featuring matrix grains, (b) XZ section featuring matrix grains, (c) XZ section with primary particle types I fine ($<0.25 \mu m$), II large (0.5 to 4 μm particles and/or agglomerates of the finer particles), and III large Nb-rich spherical particles, (d) lower magnification XY section with defects, and (e) micrograph and corresponding energy-dispersive X-ray spectroscopy (EDS) line scan.

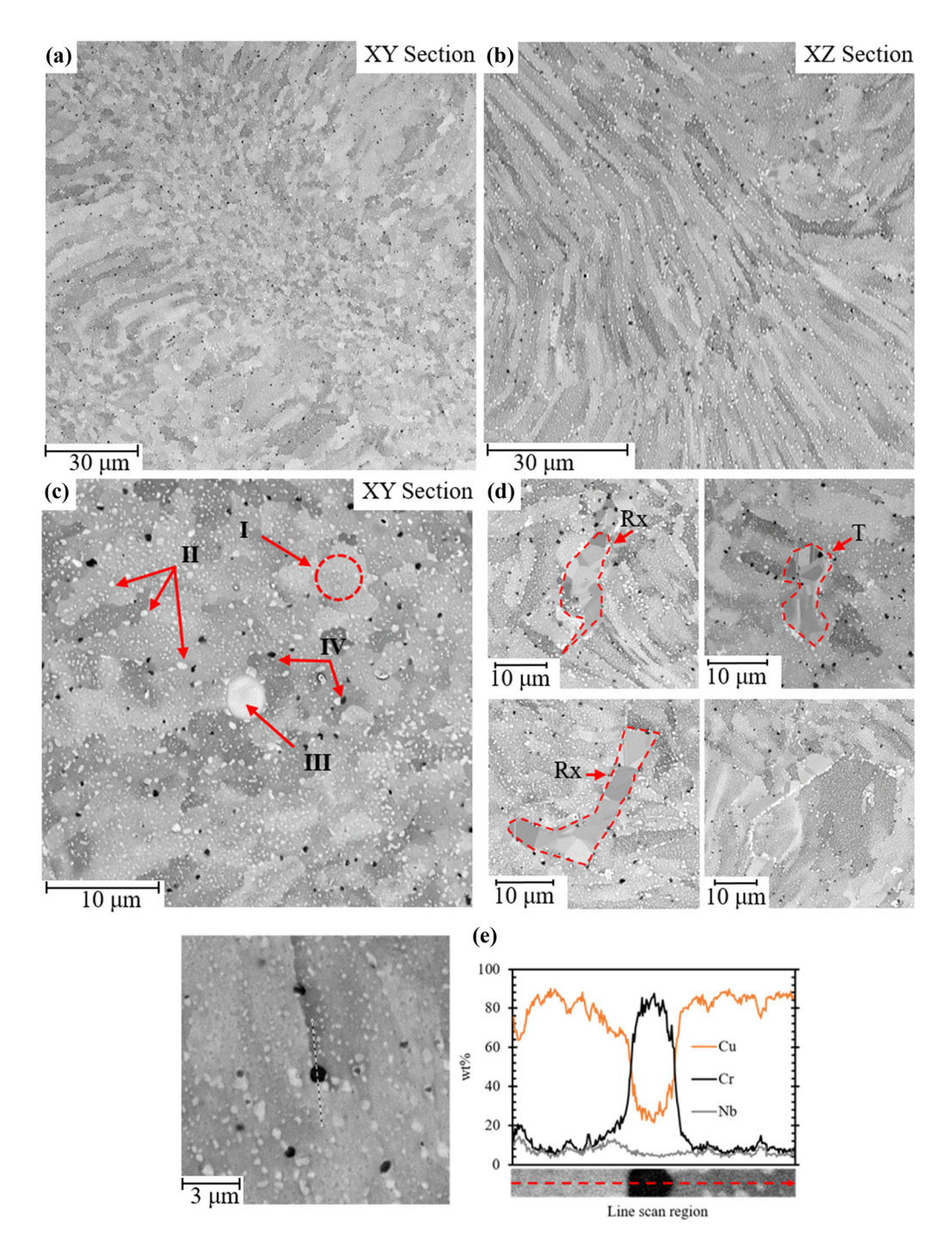


Fig. 3—SEM images for the HIPed samples (a) XY section featuring matrix grains, (b) XZ section featuring matrix grains, (c) XY section with primary particle types I, II, III, and IV, (d) images showing annealing twins and recrystallized regions, and (e) micrograph and a corresponding energy-dispersive X-ray spectroscopy (EDS) line scan.

B. Electron Backscatter Diffraction (EBSD)

1. As-built samples

Inverse pole figure (IPF) maps generated from EBSD measurements are shown in Figure 4. The selected IPF maps are parallel to the build direction to maintain consistency between the grain orientations. In the case of the XY cross sections Figures 4(a), (b), the coordinate system is the same as the IPF orientations in X, Y, and Z (build direction). Therefore, the IPF map that is parallel

to the build direction for the XY section is IPF-Z and IPF-Y is parallel to the XZ section. The Cu matrix grains were clearly resolved, compared to the particles that were unindexable and appear as small black dots at grain boundaries and within grains. Since the crystallographic information for the various particles cannot be determined from the current EBSD data, it is difficult to distinguish these particles (marked 'P') from voids (marked 'V'), build defects, and grain boundaries that

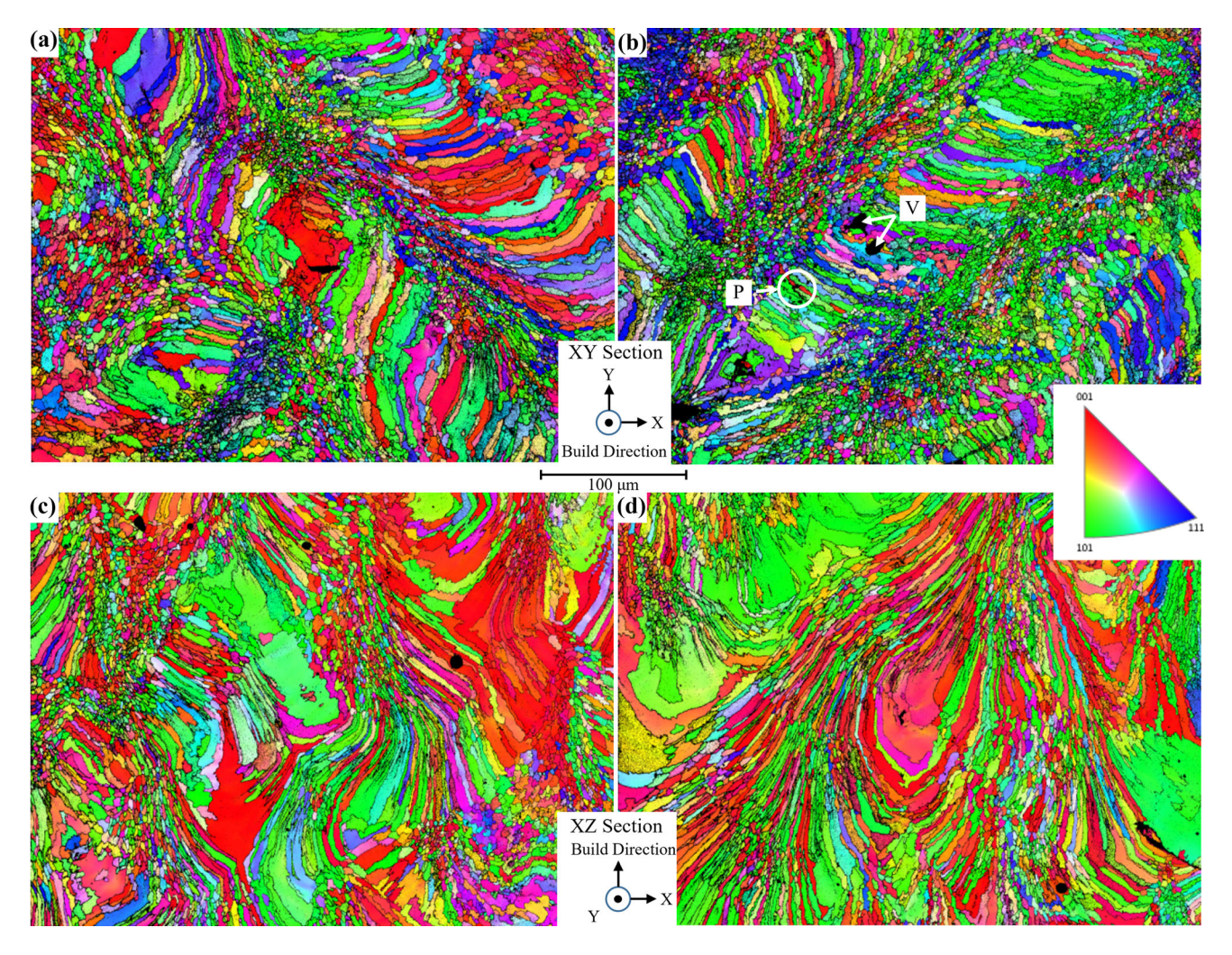


Fig. 4—Inverse pole figure (IPF) maps for as-built L-PBF GRCop-84 (a), (b) IPF-Z of the XY sections and (c), (d) IPF-Y of the XZ sections. Voids (V) and particles (P) are marked in Fig. 4b.

also appear as dark regions in Figure 4(b). Additional backscattered images were collected in parallel and showed that the larger black areas marked 'V' in Figure 4(b) in the IPF map, are voids. Although the matrix grains are visible under SEM, EBSD images better reveal the weld-line-like features. There appear to be distinct regions in the XY section [Figures 4(a), (b)] of both long curved columnar grains along the laser melt path and smaller misoriented grains in between these columnar grains. These columnar versus equiaxed regions are identified in section 4.5 (see Figure 11) and discussed in reference to the laser path. Along with images from the XZ section [Figures 4(c), (d)], we conclude that some small misoriented grains could be classified as equiaxed grains with large crystallographic misorientations between them. However, the XZ section reveals that a significant fraction of the small grains extend into thin columnar grains, so overall, the microstructure appears mixed with a columnar bias.

The corresponding (100) pole figures are presented in Figure 5. In the case of data from Figures 5(a), (b), there are two distinct [100] that are misoriented from plane normal, i.e., the Z-direction in sample coordinates.

Considering this preference, it is unusual that the XY samples do not show a similar preference in the (100) orientation of the IPF maps. The XZ [Figures 5(c), (d)] data demonstrate preferred orientation resembling cube texture, i.e., most of the < 100 > are aligned parallel to the Z-direction which was expected for FCC Cu. The melt pool morphology is highly complex due to overlap both horizontally and vertically (Figure 1), but some of the effects of overlap appear visible within the EBSD maps. At the center of Figure 4(a), there appears to be an overlap of two laser weldments running perpendicular to each other which has a dominating (100) orientation. When the weld pools overlap in a parallel path, Figure 4(b), there does not appear to be a preference for [100] growth, though the shape of the columnar grains change. Without identifying the build height in reference to the maps, it is difficult to identify the vertical overlap of the melt pools in Figures 4(c), (d), though strong epitaxial growth is evident that may be related to overlap.

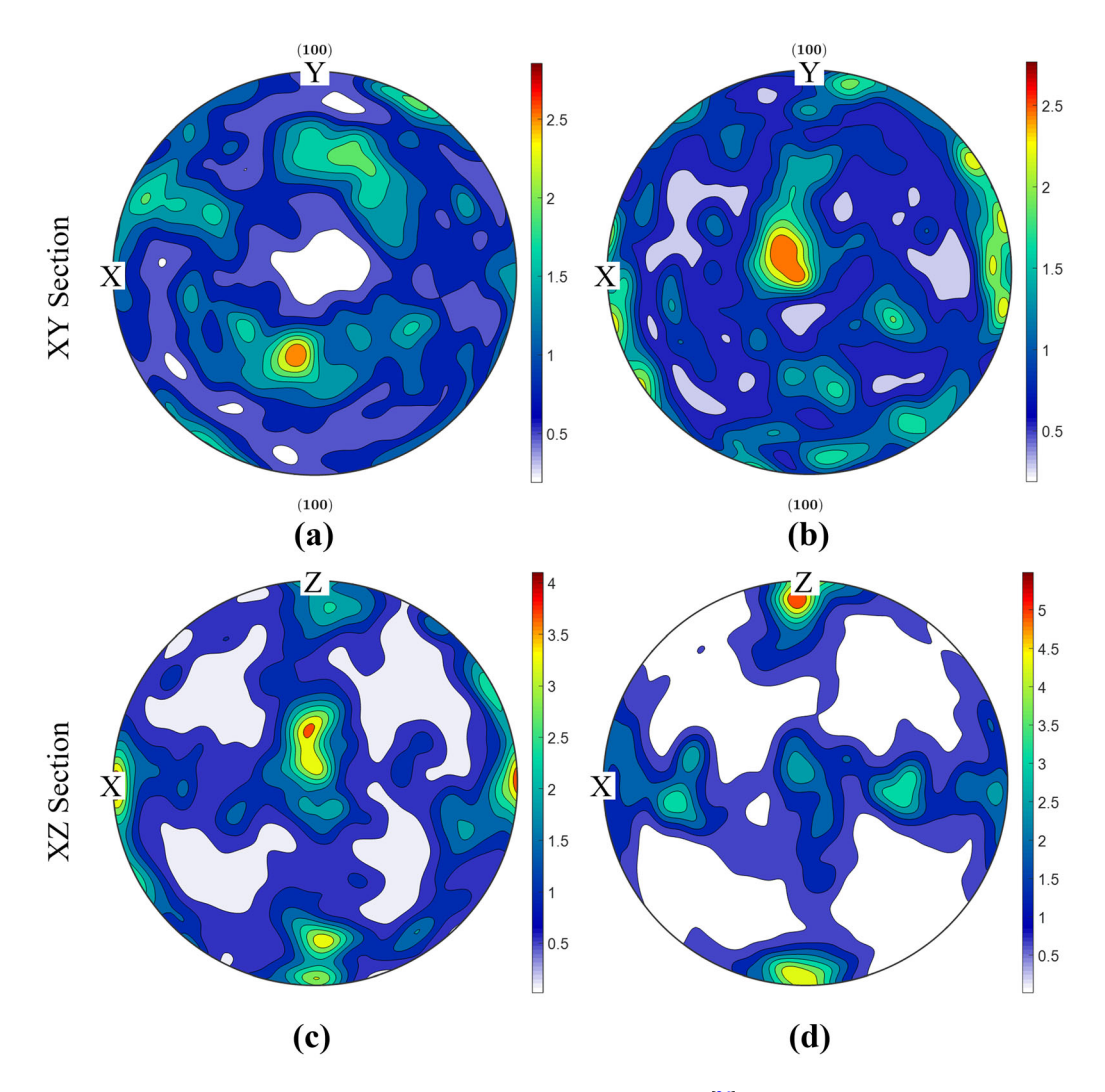


Fig. 5—(100) Pole figures of as-built GRCop-84 generated from IPF maps using MTEX^[26] (a), (b) XY cross section from Figure 4(a), (b), and (c), (d) XZ cross section from Figure 4(c), (d).

2. HIPed samples

The IPF maps and pole figures of HIPed L-PBF GRCop-84 are shown in Figures 6 and 7, respectively. The EBSD data resemble that of the Cu matrix grain structures in the as-built condition, but with generally larger grains. Despite evidence of recrystallization from the HIPed SEM images (Figure 3) which could enhance the formation of equiaxed grains from columnar grains. [32] columnar grains are still present throughout the microstructure. This may indicate that there was not a sufficient driving force to promote full recrystallization or that the high, ~ 14 vol pct fraction, based on the alloying contribution, of Cr₂Nb particles suppressed the mobility of grain boundaries. Compared to the as-built micrographs, the distinct boundaries of the melt pools from the as-built condition are less visible, similar to the SEM results. The texture of the HIPed samples is weaker compared to the as-built condition in Figure 5. Although the XY and XZ sections show preferred texture, the [100] texture is weakened compared to the as-built conditions. Considering the evidence of recrystallization in the SEM results, the grains are likely re-orienting to a lower energy state.

C. Thermodynamic Calculations and Interpretation of SEM & EBSD Results

1. Dissolution of Cr₂Nb in liquid melt pool

The precipitate sizes observed in Figure 2 Figure 3 along with the detailed characterization by Seltzman et al. [16] have shown that the Cr₂Nb particles in the powder must dissolve in superheated liquid copper and then re-precipitate in the liquid as it cools before the onset of the Cu-FCC solidification during the L-PBF process. Figure 8 shows the results of computational thermodynamic calculations using ThermoCalc® software and Copper database. Figure 8(a) shows that Cr₂Nb particles will dissolve in liquid copper if it is heated above the 1900 K. Solidification simulations, Figure 8(b), using the Gulliver-Scheil methodology, show that on cooling, the Cr₂Nb particles will precipitate out of the liquid copper first and its volume fraction will increase gradually to about 0.1 before the

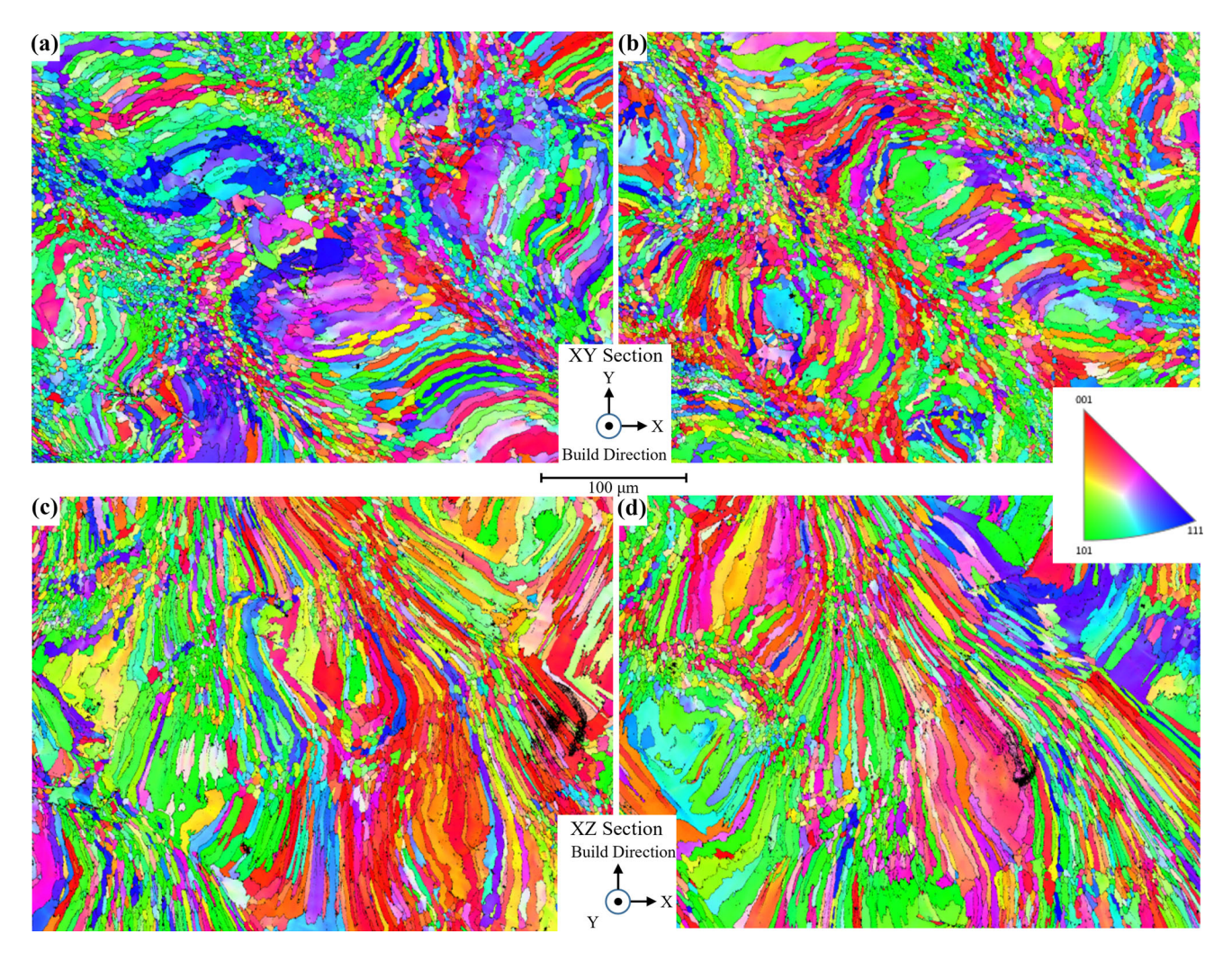


Fig. 6—EBSD maps for (a), (b) IPF-Z of the HIPed L-PBF GRCop-84 XY and (c), (d) IPF-Y of the XZ samples.

on-set of the Cu-FCC solidification. The solidification simulations also indicated that there is a potential to form Cr-rich BCC phase towards the end of solidification.

2. Melt pool characteristics

The calculated melt pool shape and temperature distributions are shown in Figure 9. The calculations used processing conditions that are typical to L-PBF and similar to the processing conditions of the as-built samples in this study. The peak temperature in the melt pool does exceed the dissolution temperature of Cr₂Nb discussed above, and some locations may experience temperatures well above the boiling point of Cu. Therefore, it is possible that the alloying element concentrations may change within the build due to preferential evaporation. Currently, however, there are no published thermodynamic and kinetic data related to the preferential evaporation of Cr and Nb from the Cu melt under L-PBF environment. However, we can conjecture on the relative evaporation by comparing the vapor pressure of pure elements. The vapor pressures of elements were calculated using the online calculator from Institute of Applied Physics (https://www.iap.tuwien.ac.at/www/surface/vapor_pressure) at 2100 K Cu is 1090 Pa; Cr is 328 Pa; and Nb is 9.20 x 10⁻⁶ Pa. With Cr present as one of the minority components, compared to the bulk presence of Cu, this suggests preferential evaporation of Cr from the melt, i.e., high vapor pressure means that it is easier to evaporate. Preferential evaporation of elements like Cr in Nickel base superalloys^[37] and Al in Ti6Al4V^[38] alloys have been reported in the literature. It evaporations occur, the local composition of Cr and Nb may reduce the extent of precipitation of these particles form the melt as it cools below the Cr₂Nb stability temperature shown in Figure 8.

The heat transfer calculations show that the melt pool shape of GRCop-84 is closer to circular than the tear-drop shape often seen during welding and additive manufacturing of other alloys. This dramatic reduction in melt pool shape and size (i.e., width 200 μ m, length 50 μ m, and depth 50 μ m compared to other metal alloys that are on the order of mm's) are attributed to the higher thermal conductivity of the GRCop-84 alloy. The calculations here used 80 pct laser absorption efficiency;

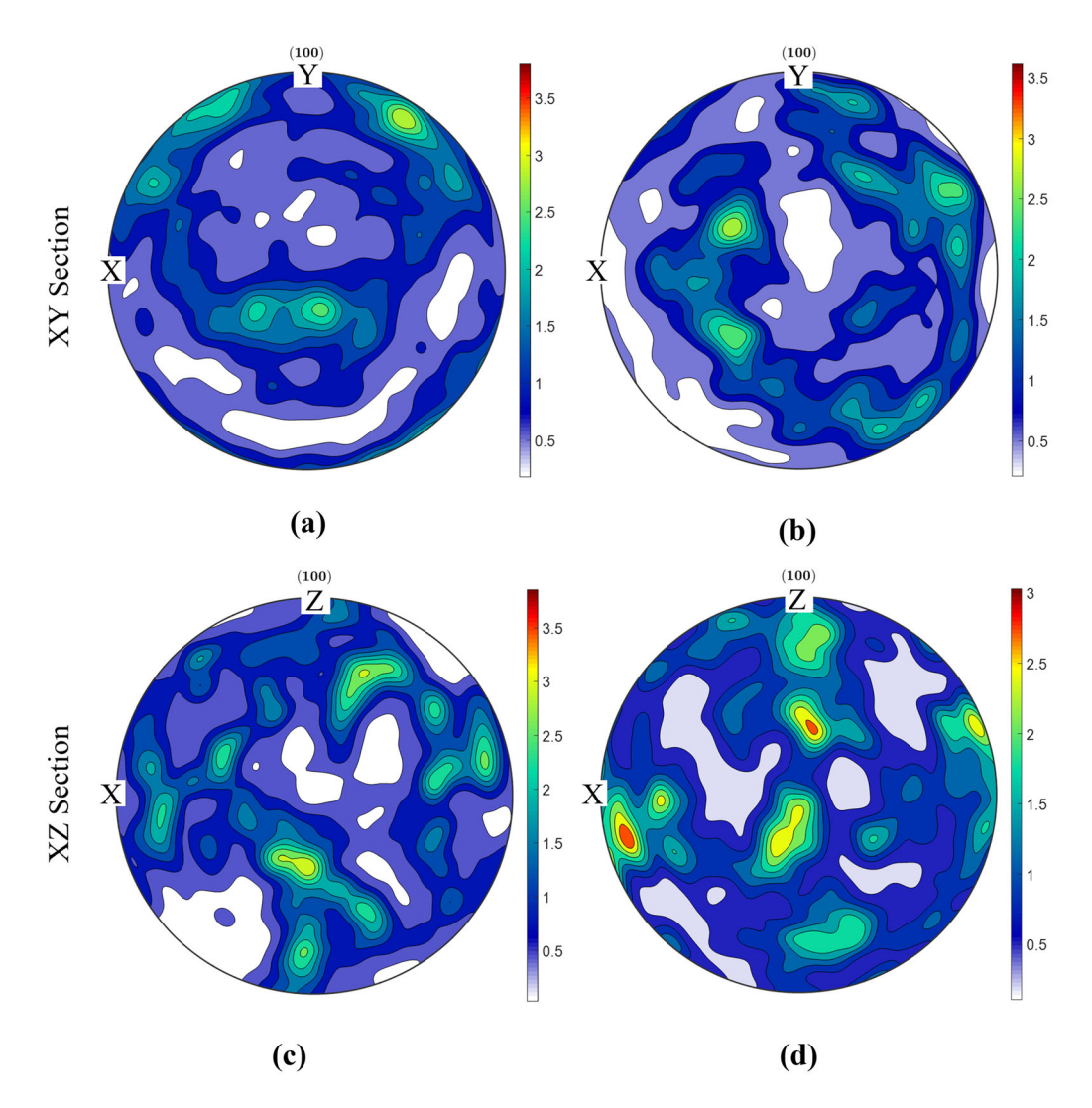


Fig. 7—(100) Pole figures of as-built GRCop-84 generated from matching IPF maps using MTEX^[26] (a), (b) XY cross section from Figure 6(a), (b) and (c), (d) XZ cross section from Figure 6(c), (d).

however, it is well known that the absorption efficiency in additive manufacturing conditions may be lower than 50 pct. [39] Under lower absorption conditions, the melt pool shape may become smaller and may not induce the evaporation. The uncertainty in laser absorption by Cu powders may trigger complex dynamics of melt pool shape with reference to the hatch distances used during L-PBF and may have large influence on the solidification grain structure. [40]

D. Grain Structure Rationalization

1. Presence of [100], [101], and [111] orientation with build direction

One observation is the lack of strong [100] crystallographic texture in L-PBF GRCop-84 builds compared to other alloy builds published in the literature as shown in Figure 10(a). This can be evaluated by considering the details of a non-planar melt pool geometry with reference to the overall build coordinate system, laser coordinate system, and geometry of sectioning the samples. The [100] solidification texture will align with

the maximum thermal gradient vector within the melt pool so a strong [100] texture is expected if the gradient coordinates match with build coordinates. However, careful analysis of the surface of the L-PBF builds confirms that the surface is not planar, so the above assumption may be invalid and leading to the spatial rotation of the melt pool shape with reference to sample coordinates, Figure 10(b), as it navigates the rough surface. In addition, uncertainty was introduced during sectioning of the samples for the EBSD measurements. The interaction of stationary and dynamic coordinates is schematically illustrated in Figure 10(c).

The above effect can be visualized by overlaying soft noodles (i.e., representing each laser melt bead) in a periodic fashion (i.e., representing the hatch distance) corresponding to n^{th} layer. Next the second set of soft noodles in the $(n+1)^{th}$ layer at 90 deg to the noodles in the n^{th} layer is overlayed. Figure 10 highlights that the dynamic nature of the maximum thermal gradient coordinate system or the alignment of [100] crystallographic orientation will oscillate with reference to the stationary build or sectioning coordinate. The above

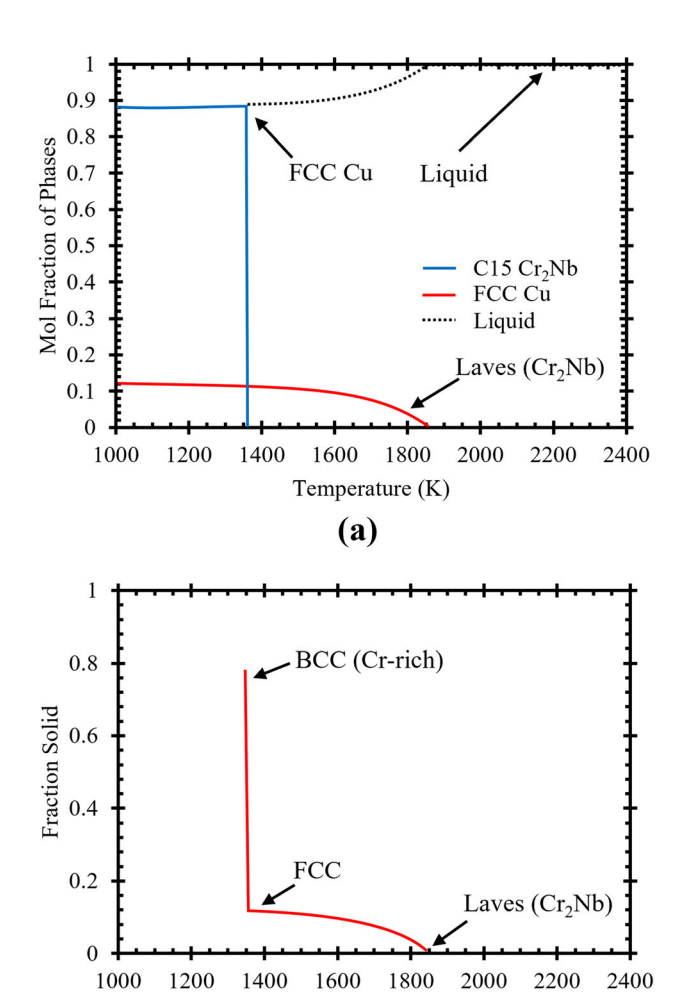


Fig. 8—Thermodynamic calculations: (a) phase fractions as a function of temperature under equilibrium conditions; (b) Gulliver-Scheil solidification simulation showing the sequence of phase evolution during cooling.

Temperature (K)

(b)

discussion indicates that the interpretation of the EBSD images in highly conductive metals with a small melt pool requires in-depth analysis of the melt pool coordinates, maximum thermal gradient vectors, surface roughness, and orientation of the melt pools with reference to build geometry and sectioning methods.

Some of the effects of overlap appear visible within the EBSD maps. At the center of Figure 4(a), there appears to be an overlap of two laser weldments running perpendicular to each other which has a dominating (100) orientation. Similarly, the XZ maps, Figures 4(c), (d) show large regions dominated by [100] oriented grains which could be the result of overlapping weldments and strong epitaxial growth. When adjacent, horizontal weld pools overlap, there does not appear to be a preference for [100] growth, though the shape of the columnar grains changes; Figure 4(b) provides the best example of this observation.

E. Columnar to Equiaxed Transition During Solidification

The EBSD image in Figure 11(a) shows the presence of small Cu-FCC equiaxed grains in between the Cu-FCC columnar grains. The exact location of these regions with respect to melt pool shape and size is not known; however, the expected position of the equiaxed and columnar grains with respect to the laser path is proposed based on the welding literature, i.e., columnar grains near the boundaries of melt pool with large thermal gradients and equiaxed grains near the center of the melt pool regions. [21,22,42] The above conditions will lower the activation energy for nucleation of equiaxed grains and agrees with Villafuerte et al.[43] Another important factor for columnar to equiaxed transition (CET) is the presence of appropriate G and R conditions. The above conditions were evaluated by coupling a simple heat transfer model with models of columnar to

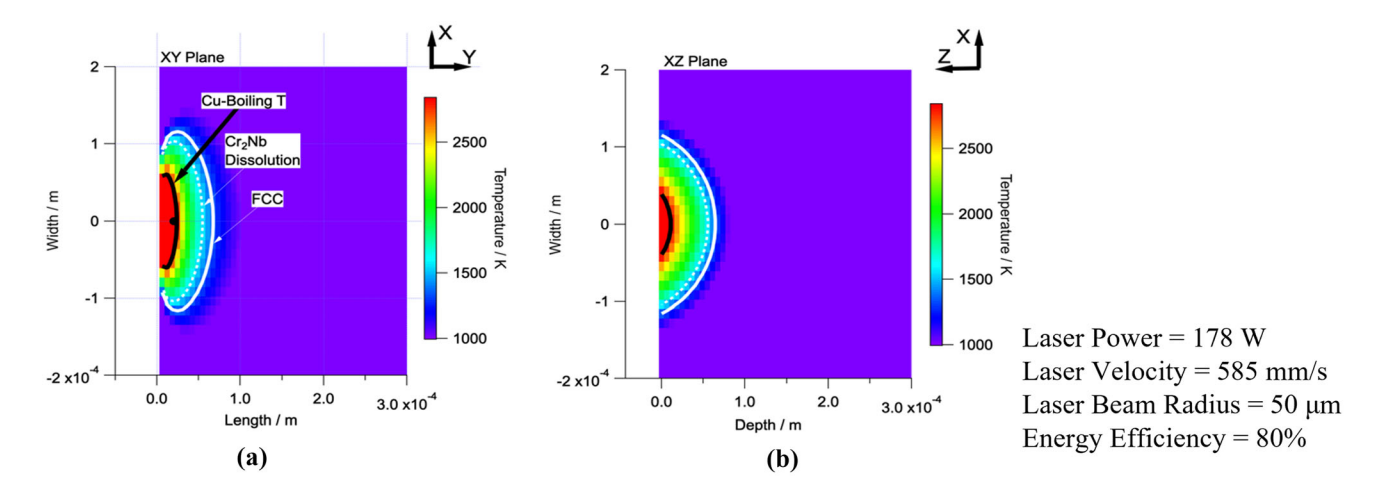


Fig. 9—Calculated melt pool shapes and temperature distributions (a) XY and (b) XZ sections using the modified Rosenthal equation. The contour lines correspond to boiling point of Cu (black), dissolution temperature of Cr₂Nb, and complete dissolution of Cu-FCC phase (white).

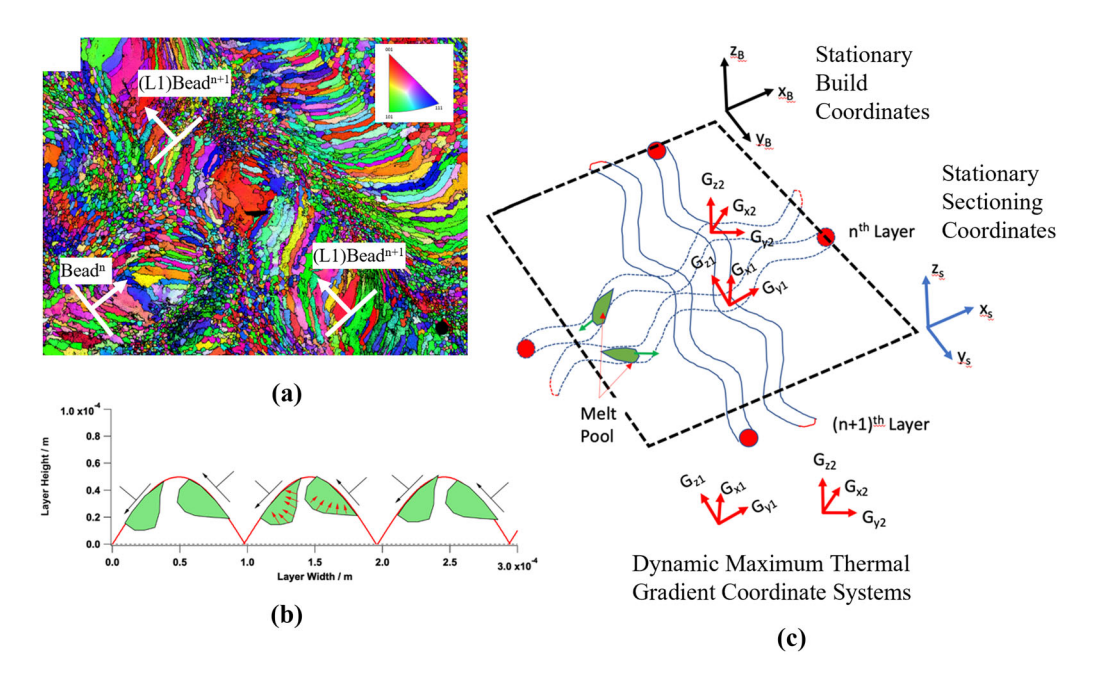


Fig. 10—Rationalization of [100], [101], and [111] crystallographic orientation with reference to build coordinates: (a) EBSD image showing non-planar laser bead geometry in the $(n + 1)^{th}$ layer due to periodic surface roughness introduced in the n^{th} layer. (b) Schematic illustration of melt pool in the $(n + 1)^{th}$ layer navigating the surface roughness created during n^{th} layer. The black arrows show the motion of the weld pool and the red arrows in some melt pools (green) indicate the orientation of the maximum thermal gradients, and (c) schematic description of the interaction between static (build and sectioning) coordinate system and dynamic maximum thermal gradient coordinate system in three dimensions (Color figure online).

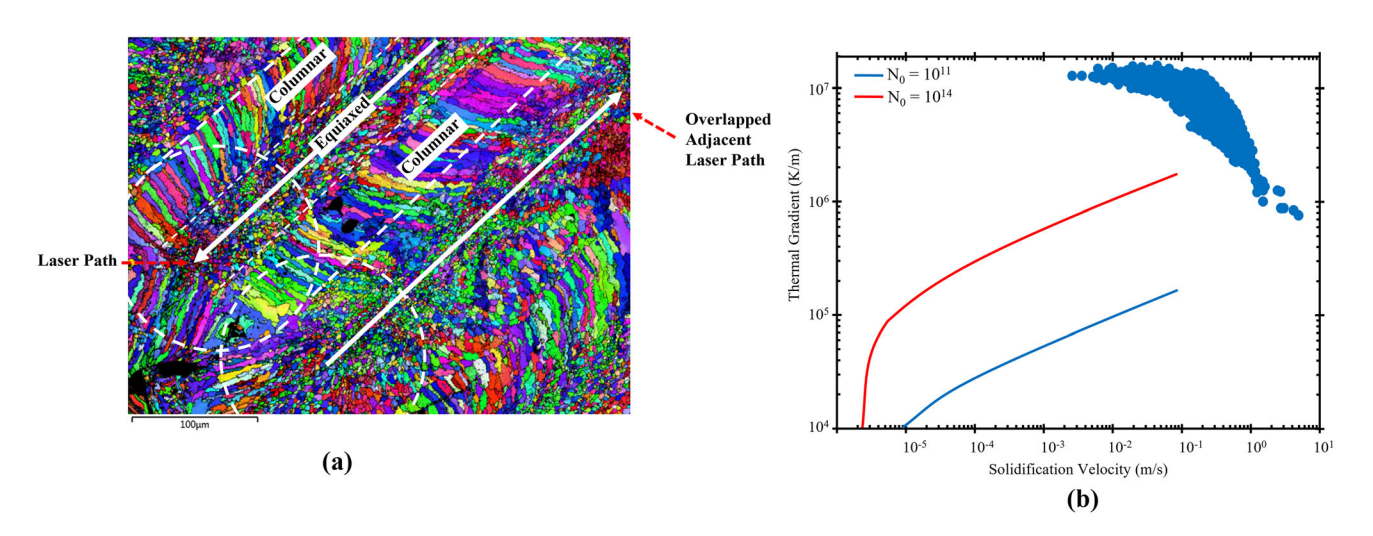


Fig. 11—(A) EBSD image revealing regions of columnar and equiaxed grains; (b) calcualted columnar to equiaxed transition (CET) for GRCop-84 alloy composition overlaid with calcualted G and R for the L-PBF processing conditions.

equiaxed transition. [29] One of the key requirements for the equiaxed grains is the number density of nucleating particles (N_0 in the units of m^{-3}) in the liquid melt coupled with appropriate thermal gradients (G) and liquid–solid interface velocity (R) Figure 11(D). For GRCop-84 the Cr_2ND that may form in the liquid melt pool (> 10 vol pct) could provide a high number density of heterogenous nucleation sites. The results show that for the sets of G and R calculated for the current L-PBF processing conditions, it is difficult to induce columnar to equiaxed transition due to high thermal gradients.

Even by increasing the N_0 values by three orders of magnitude (10^{11} to 10^{14}), the CET transition lines do not intersect the calculated G and R values based on heat transfer models. If we consider typical microstructures in Figure 2(d) with high concentration of Cr_2Nb particles (in region I), the approximate number density of the particles per unit area is estimated to be 6.25 x 10^{10} m⁻² (10 particles within a small rectangular area of $80~\mu m$ and $2~\mu m$). By assuming a section thickness for the optical microscopy to be $2~\mu m$, the number density of Cr_2Nb particles may reach up to $3.125~x~10^{16}~m^{-3}$.

However, this number density of particles should be present closer to the liquid-solid boundary and within a small volume defined by the dendrite tip radius of sub- μ m. Achieving 10^{14} m⁻³ particles close to a dendrite tip radius of 0.1 μ m will be difficult. Although there are subtle changes in the distribution of Cr₂Nb particles across the melt layer, currently, we do not have a method to estimate the spatial distribution of these particles with reference to the melt pool geometry (boundary or center) or build geometry. These data also suggest that the 3D distributions of Cu-FCC grain size, shape, and crystallographic texture is necessary to understand the complexities of the FCC grain evolution during typical L-PBF condition.

Furthermore, the high G (> 10^6 K/m) values eliminate the possibility of stabilizing the dendrite growth at velocities (R) greater than 0.1 m/s and may induce planar growth. The onset of planar growth at high liquid–solid interface velocity is also expected to induce solute trapping during solidification. This leads to the hypothesis: if the kinetics of Cr_2Nb precipitation in liquid melt is delayed until it reaches the FCC solidification temperature, and under trapping conditions, the Cu may become supersaturated with Cr and Nb. Further work is necessary to confirm this hypothesis.

F. Grain Misorientation Evolution During HIP

Due to the high degree of crystallographically misoriented Cu-FCC boundaries and locked in dislocation density, rapid recrystallization and grain growth during post-process HIP treatment are expected. [45] Some amount of recrystallization (Figure 3) was observed; however, the reduction in the [100] crystallographic orientation appears to be significant. It is well known that reduction of certain orientation distribution during grain growth is related to grain boundary velocity. The grain boundary migration velocity (v) in general is related to mobility (M) and the driving force (Δf) as through the relationship $v = M\Delta f$. The literature has shown that the mobility of grain boundaries is sensitive to crystallographic characteristics of these boundaries, [46,47] and therefore, to energies of grain boundaries created during L-PBF processing. The grain boundary energies of symmetric tilt grain boundaries (STGB) and asymmetric tilt grain boundaries (ATGB) have been published by Tschopp and McDowell. [48] The data were extracted and compared in Figure 12 for pure Cu and assumes no segregation of impurities.

The data show the tilt boundaries, created by the misorientation with reference to [100] axis, do have higher energies compared to the tilt boundaries created by [110] misorientation axis. We propose that the high energy grain boundary orientations with [100] axis will be replaced by low-energy grain boundaries with the [110] misorientation axis. Another factor that may play an important role is related to the presence of Cr₂Nb at the grain boundaries, Figure 3(d) that may allow for particle-stimulated recrystallization^[49] and pinning of the grain boundaries by particles. ^[50] This result shows a potential approach for grain boundary engineering ^[51] in complex components made by additive manufacturing.

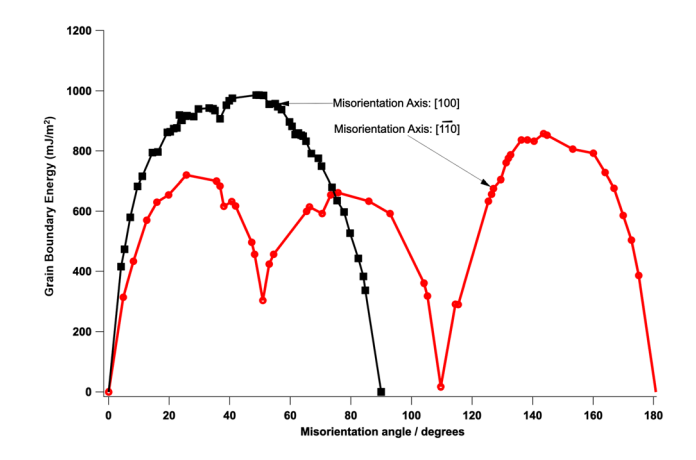


Fig. 12—Comparison of published^[48] grain boundary energies for Cu grain boundaries with different misorientation axis-angle pairs.

The tendency for defect formation is attributed to thermal gradients and lack of time for the melt pool to reach equilibrium due to thermal conditions at the edges of the build^[52] and the small, rapidly cooling melt pools created in copper builds due to high thermal conductivity.

G. In situ High-Temperature X-ray Diffraction

1. Gas-atomized powder samples

X-ray powder diffraction data, collected on the as-received gas-atomized powder, before, and after heating to 1123 K are shown in Figures 13(a), (b). In Figure 13(c), the data collected at 1123 K and after cooling back down to 298 K are compared, the peak shift due to thermal expansion is apparent. Prior to heating, a weak diffraction peak at 38.8 deg deg 2θ attributed to BCC Nb is visible. At 1123 K and after cooling, the intensity of this peak increases and the peak sharpens suggesting a decrease in disorder, microstrains, and/or an increase in crystallite size. Refinement results determined that 0.9(3) wt pct of BCC Nb is present after heating and cooling back to room temperature. Any free BCC Nb is unexpected since GRCop alloys have a slight excess of Cr to prevent the formation of the Nb phase by lowering its activity and consuming the Nb in forming Cr₂Nb. [53] The presence of free Nb is supported by the observance of Nb-rich particles revealed in the SEM images of the as-built samples (Figure 2). The presence of BCC Nb in the powder could be explained by the solidification rate being so rapid that the BCC Nb is able to form through significant partitioning of the elements. However, this is unlikely based on the preferential formation of Cr₂Nb and also due to the thermal history of gas atomization. Under gas atomization conditions, initial cooling is rapid. However, once the outer shell of the particle has solidified, the cooling rate at the core of the particle decreases significantly due to the insulative effect of the outer shell reducing the chances for significant segregation. A second and more plausible explanation could be that Cr from the potentially supersaturated Cu matrix may partition to form a solid solution with BCC Nb.

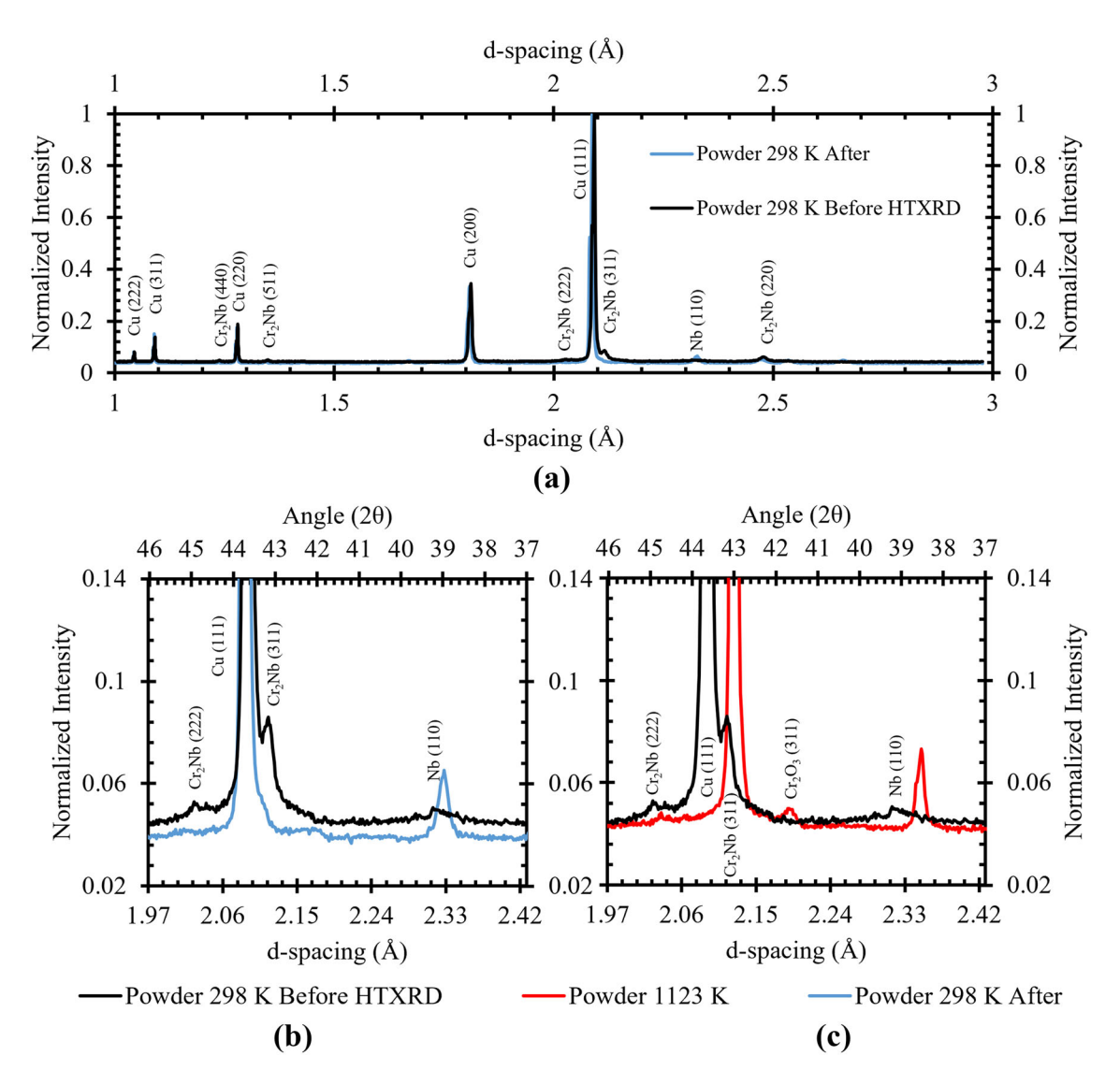


Fig. 13—Normalized X-ray diffraction data of as-received gas-atomized GRCop-84 powder (a) 30 to 100 deg 2θ comparing data collected at room temperature before and after heating to 1123 K, (b) detailed view between 37 to 46 deg 2θ , (c) detailed view between 37 to 46 deg 2θ comparing data collected before and at 1123 K.

Using the data collected initially at room temperature, the amount of initial Cr₂Nb was refined to be 7.2(3) wt pct, significantly below the 11.6 wt pct expected from the alloy chemistry. The rapid solidification experienced during gas atomization could give rise to small Cr2Nb crystallite sizes and disorder. Either of these two factors would produce broad, low intensity Cr₂Nb peaks, resulting in the low-phase fraction result. A significant fraction of the Cr₂Nb particles in gas-atomized GRCop-84 are between 10-100 nm.^[1] The Scherrer equation shows an inverse relationship between crystallite size and peak broadening and for particles of this size the diffraction maxima are broad and diffuse. [54] Disorder could be attributed to the rapid solidification potentially quenching in non-equilibrium states or defect structures and micro-stresses also resulting in peak broadening.^[53]

The previous explanation for the free Nb content that a significant amount of Cr from the Cu matrix may partition to form a solid solution with BCC Nb, could also support the relatively low Cr_2Nb phase fraction that increases at high temperatures due to the Cr_2Nb rejecting Nb for a more favorable stoichiometry. The amount of dissolved elemental content within the BCC $Nb_{1-x}Cr_x$ could be estimated using the refined lattice parameters for BCC and applying Vegard's law. [55] However, there is a high probability of micro-strains in the gas-atomized powder that also influence the lattice parameter and the two factors cannot be easily deconvoluted. [54] In the future, the degree of solute present in the matrix could be assessed by atom probe tomography. [56,57]

When heated, the powder readily oxidized, demonstrated by the emergence of additional weak diffraction peaks. These were difficult to identify due to low intensity and overlap with other peaks but are likely Cr and Nb-based oxides. These additional phases complicate quantitative determination of the phase fractions at higher temperatures.

2. As-built GRCop-84 L-PBF samples

Power diffraction data collected on the as-built sample are shown in Figure 14. Figure 14(a) shows the data between 30 and 100 deg 2θ and Figure 14(b) shows a detailed comparison between 40 and 46 deg 2θ at room temperature before heating and after heating to 1223 K and cleaning the surface. Figure 14(c) shows a detailed comparison between 40 and 46 deg 2θ at room temperature prior to heating before and at 1223 K. At 1273 K, two minor Cr₂O₃ peaks are present. Significant oxidation occurred, requiring the specimen be cleaned of surface oxides with a high grit grinding pad and water, providing a method of assessing the bulk composition without interference from oxides. A comparison of the refined lattice parameters and phase fractions at room temperature prior to and after heating to 1223 K, for both the as-built and HIPed samples are provided in Table II. The phase fraction and lattice parameters of Cr_2Nb in the as-built samples prior heating to 1223 K are difficult to confidently determine to due to the low intensity of the peaks, similar to gas-atomized powders. Following heating to 1223 K, the Cr_2Nb peaks sharpen and the refined amount of Cr_2Nb increases to 11.7(6) wt pct which is approaching the amount expected based on the alloy design. The peak sharpening could be attributed to annealing out disorder, micro-strains, and/or the Cr_2Nb particles experiencing crystallite growth.

Prior to heating, no free Cr is observed in the as-built sample, however, after heating 0.6(4) wt pct of Cr was refined. This supports the SEM/EDS results indicating that free Cr is present in the HIPed samples but not the as-built samples and that heating is required for an observable amount of the free Cr to precipitate, and at higher temperatures, the free Cr at the surface readily oxidizes. In contrast to the gas-atomized powders, there

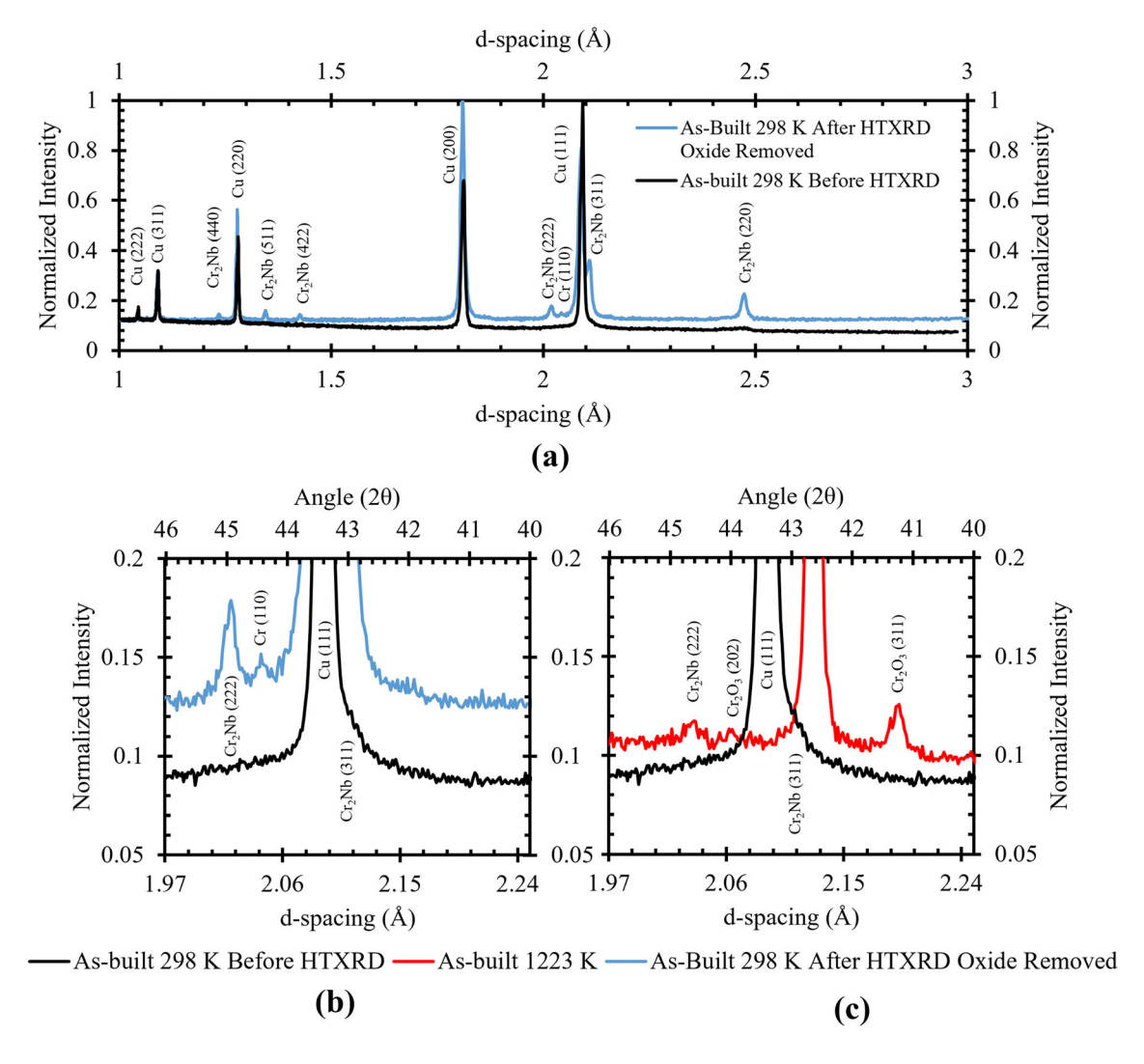


Fig. 14—Normalized X-ray diffraction data of as-built L-PBF GRCop-84 samples sectioned from larger parts (a) 30 to 100 deg 2θ comparing data collected at room temperature before and after heating to 1223 K, (b) detailed view between 40 and 46 deg 2θ , and (c) detailed view between 40 to 46 deg 2θ comparing data collected before and at 1223 K.

Table II. The Lattice Parameters and Phase Fractions (Wt pct) for Each Investigated Condition of GRCop-84 Samples Before and After Heating to Maximum Temperature; Oxide Surface Layer was Removed from the As-Built and HIPed Samples Prior to XRD; esd Reported as (3σ)

	Prio	or to Heating		After Heating	
Condition	Cu	Cr ₂ N	b	Cu	Cr ₂ Nb
Powder a (Å) wt pct	3.6229(5) 92.7(9)	7.3(6)		3.6158(3) 98.5*	6.990(1) 1.5*
	Cu	Cr ₂ Nb	Cu	Cr ₂ Nb	Cr
As-Built a (Å) wt pct	3.6235(1)* 99.1(7)	6.99** 0.8**	3.6208(2) 87.7(9)	6.997(2) 11.7(6)	2.89(1) 0.6(4)
	Cu	Cr ₂ Nb		Cu	Cr ₂ Nb
HIP a (Å) wt pct	3.6189(3) 90(1)	6.994(2 10.2(7)		3.6141(3) 89.8(1)	

^{*}Note significant oxidation decreases relative contribution of Cr2Nb.**Estimated due to low intensity, broad and superimposed peaks.

is no detectable free BCC Nb. This suggests that the melting and solidification cycles in L-PBF move the general stoichiometry to a state where excess Cr is present and Nb is consumed into Cr_2Nb .

3. HIPed GRCop-84 L-PBF samples

Powder diffraction data collected on the HIPed sample are shown in Figure 15. Figure 15(a) shows the data between 30 and 100 deg 2θ , and Figure 15(b) shows a detailed comparison between 40 and 46 deg 2θ at room temperature before heating and after heating to 1223 K and cleaning the surface. Figure 15(c) shows a detailed comparison between 33 and 41 deg 2θ at room temperature prior to heating before and at 1223 K. Prior to heat heating, the data showed a small diffraction maximum, barely distinguishable above the background in Figure 15(b), at approximately 44.5 deg 2θ , which most closely matches the (110) reflection of BCC Cr and agreeing with the SEM/EDS results that indicated Cr-rich particles, Figure 3. At 1273 K, Figure 15(c), there are Cr₂O₃ peaks, suggesting the BCC Cr oxidized, and some low intensity NbO₂ peaks. The data suggest that significant oxidation occurred, similar to the as-built samples, and again requiring specimen be cleaned of surface oxide.

A comparison of the refined lattice parameters and phase fractions at room temperature prior to and after heating to 1223 K is provided in Table II. Accurate Rietveld refinements are difficult in this alloy system due to significant overlap of the diffraction peaks and limited diffraction intensity of the minor phases, and the presented values are primarily intended for comparison rather than accuracy. For example, Cr is only included in the as-built condition after heating in Table II which was the only case where a reliable refinement could be completed. Cr is also present in the

HIPed sample prior to heating, shown in Figure 15, but its contribution could not be reliably calculated.

After heating to 1223 K and cooling, the phase fractions and lattice parameters of the HIPed condition in Table II remains largely unchanged, demonstrating the stability of Cr_2Nb after HIPing. The refined phase fractions of Cr_2Nb , 10.2(7) and 10.2(8) wt pct, in the HIPed samples at room temperature are statistically identical prior to and after heating, respectively. This is significantly higher than that observed in the as-built sample prior to heating but within 3σ of the wt pct of Cr_2Nb after heating. The higher phase fraction amounts of Cr_2Nb for the as-HIPed sample is approaching the amount expected based on the alloy design.

4. In Situ HT XRD

In situ data of the high-temperature XRD of the powder, as-built, and HIPed conditions are presented in Figure 16 as a function of time. The intensity of both the primary Cu and Cr₂Nb reflections were analyzed to provide information about the stability of the Cr₂Nb precipitates and the FCC grain structure and are compared during the heating cycle. The diffraction data were collected using different incident and diffracted beam optics conditions to maximize intensity in some cases, in order to compare across the different samples, the Cu-FCC (111) peak intensity in each experiment was used to normalize the data. The intensity is indicated by color while the y-axis indicates the time as the temperature was ramping (see right inset).

The (311) is the strongest reflection for Cr_2Nb ; however, due to its proximity to the strong Cu (111) and depending on the temperature, it could be difficult to resolve. The Cr_2Nb (220), at approximately 36 deg 2θ , was used to indicate the presence of Cr_2Nb , and while the presence of this peak is well defined in the

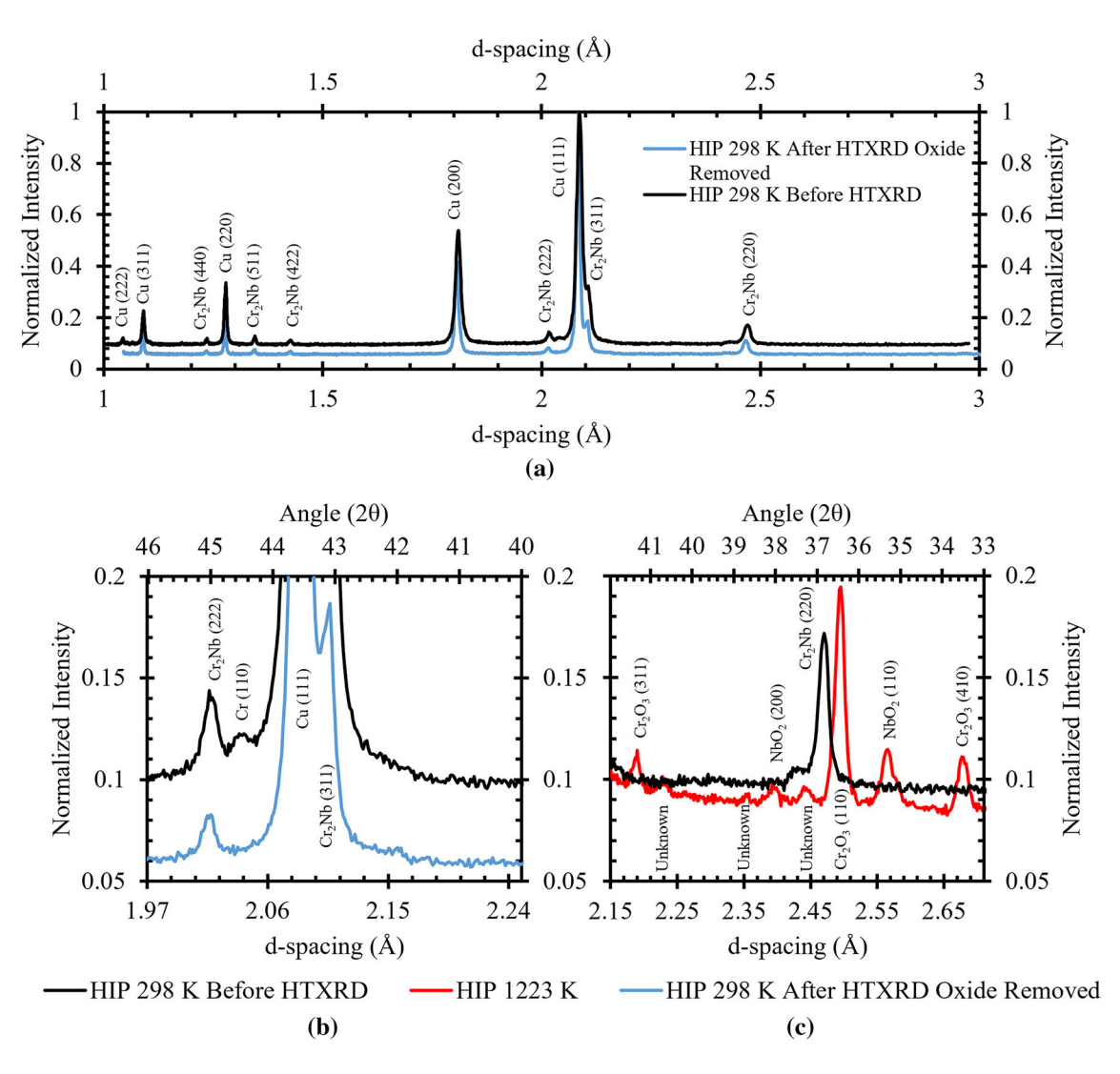


Fig. 15—Normalized X-ray diffraction data of HIPed L-PBF GRCop-84 samples sectioned from larger parts (a) 30 to 100 deg 2θ comparing data collected at room temperature before and after heating to 1223 K, (b) detailed view between 40 to 46 deg 2θ , and (c) detailed view between 40 to 46 deg 2θ comparing data collected before and at 1223 K.

gas-atomized powder and HIPed samples, the intensity in the as-built condition was barely present above background. However, on heating above the 838 K, the Cr₂Nb peaks of the as-built sample sharpen and can be unambiguously indexed. The apparent change in crystallinity of the Cr2Nb could be due to a variety of responses that are difficult to deconvolute. The microscopy results identified particles distinct from the matrix in the as-built condition that were rich in Cr and Nb. This suggests that the change in crystallinity after heating is not due to precipitation of Cr and Nb that was dissolved in the Cu matrix and further precipitation is unlikely. The particles could instead have undergone a stoichiometry change, reduction of interparticle strain, or coarsening above the detection limit. Neutron diffraction experiments support the results above and will be published elsewhere.

Figure 17 compares changes in the lattice parameters calculated from the Cu (111) and (200) for the

gas-atomized powder, as-built, and HIPed samples at each temperature, along with the lattice parameters obtained from the longer datasets collected at room temperature prior to and post-heating. A slope change between 473 and 873 K is apparent for both the gas-atomized and as-built samples in Figures 17(a), (b), respectively; however, the data collected on the HIPed sample in Figure 17(c) does not display the slope change and only follows one slope. For the gas-atomized powder and the as-built sample below 473 K and above 873 K, the relationships between the lattice parameter and temperature are linear. For both the gas-atomized powder and the as-built samples, the lattice parameter obtained from the larger dataset collected prior to heating agrees well with the lower temperature range slope and the lattice parameter obtained from the larger dataset collected post-heating agrees well with the higher-temperature range slope. Confidently understanding the origin of this lattice

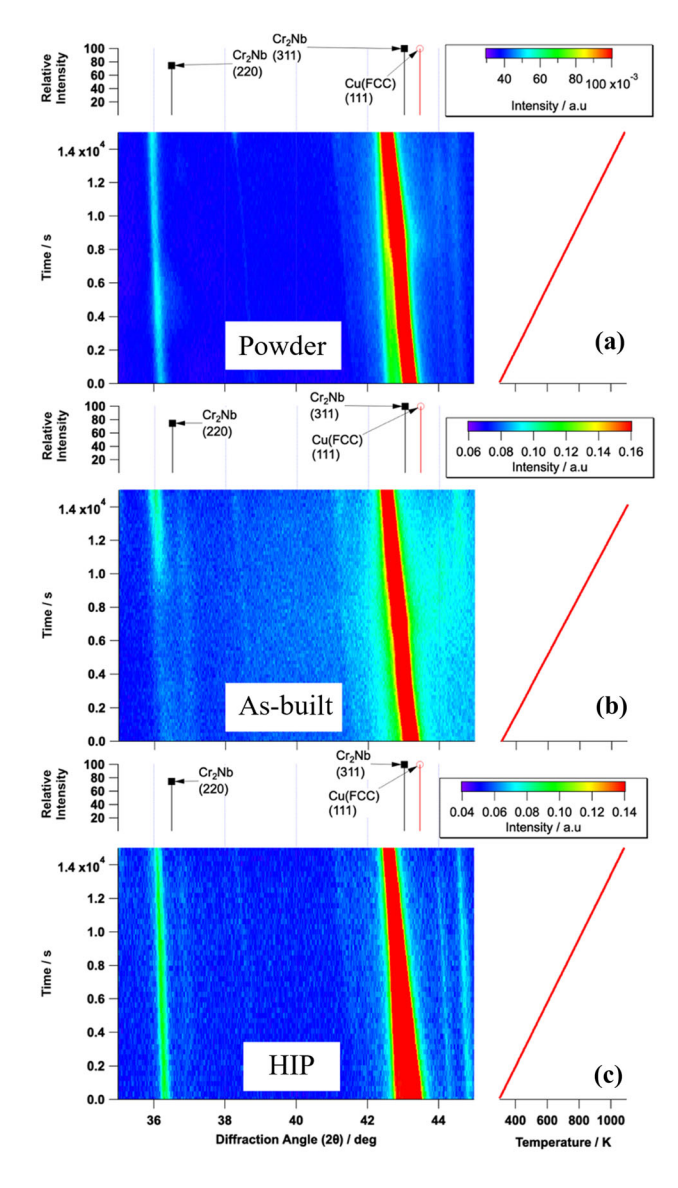


Fig. 16—Normalized X-ray diffraction intensity as a function of time and temperature during heating cycle: (a) as-received gas-atomized powder; (b) as-built and (c) HIPed samples. The Cu-FCC (111) peak intensity in each experiment was used to normalize each dataset. However, different intensity scales (see color bar top right) were used to highlight the presence of $\rm Cr_2Nb$ diffraction in all samples (Color figure online).

change is difficult since multiple factors could be contributing including changes in the composition and the annealing resulting in the relief of residual thermal stresses. It is apparent that the gas-atomized powder and as-built samples may have residual stresses which are relieved on heating above the 873 K, in agreement with the annealing range described in literature, and Cr₂Nb precipitates. In contrast, the HIPed sample appears to have consumed all recrystallization or compositional change potential within the tested temperature range. Residual stresses with the microstructure should be low and the microstructure should remain stable unless sufficient time or temperature exceeds the potential.

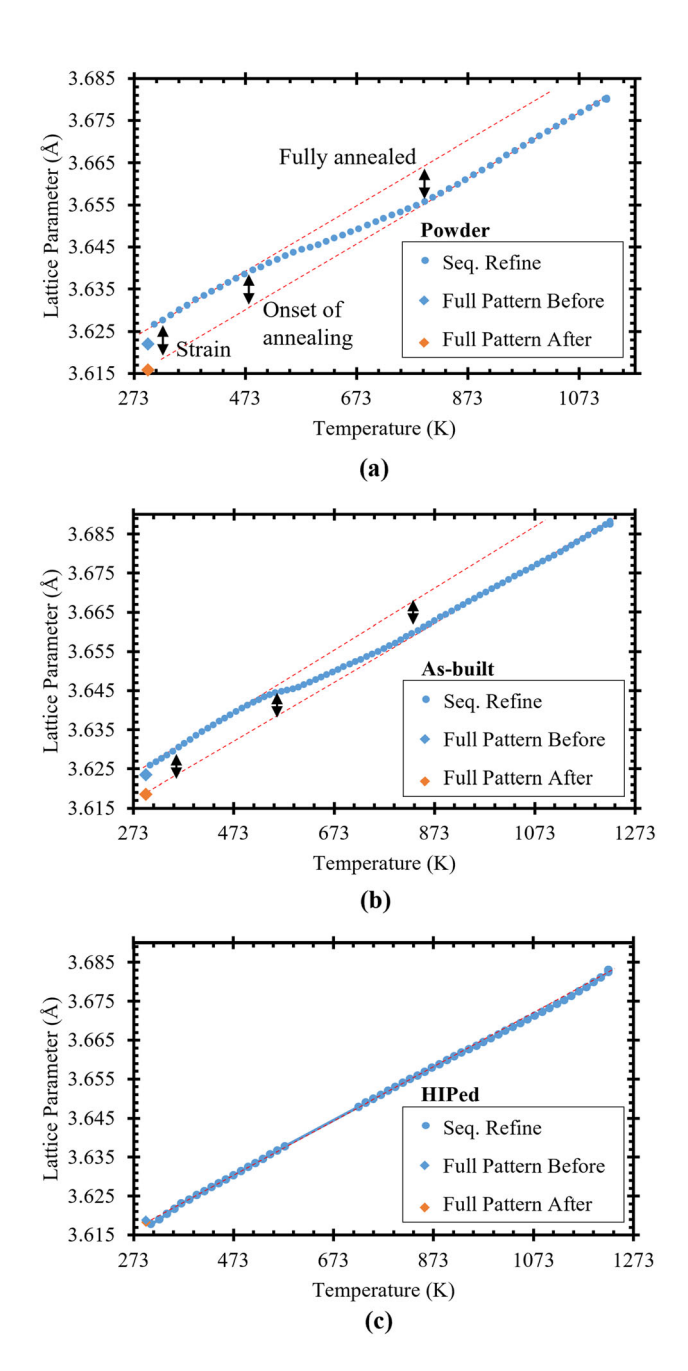


Fig. 17—Cu lattice parameters determined from HTXRD data for (a) gas-atomized powder, (b) as-built, and (c) post-HIPed samples. Each figure includes the refined lattice parameter from data collected over a larger two-theta range, at room temperature prior to and after heating to 1123 K. Error bars were smaller than the data markers.

IV. CONCLUSIONS

The microstructure evolutions in GRCop-84 alloy builds made by laser-powder bed fusion process were characterized in the as-built and after hot isostatic pressing (HIP) using a suite of characterization tools. The major conclusions are

1. The as-built material showed smaller size distribution of Cr₂Nb precipitates compared to that typically present in the powder. This observation is

- attributed to dissolution and reprecipitation of Cr_2Nb into and from the liquid melt pool during heating and cooling, respectively. Some extent of coarsening of fine (10–100 nm) particles is seen following the HIP post-processing, but the larger particles remained stable.
- A heterogeneous Cu-FCC matrix microstructure consisting of both equiaxed and columnar grains, with wide range of crystallographic misorientations, is observed in the XY (perpendicular to build direction). In contrast, in the XZ (along the build direction) section, strong (100) epitaxial preferential growth is observed, and bundles of (100) columnar grains traverse multiple layers. The above solidification grain structure evolution is attributed to the dynamic orientation of the coordinates describing the maximum thermal gradient with reference to laser path direction, coordinates describing the build geometry and the sectioning plane. Relatively stable Cu-FCC grains and reduction of [100] grain orientations are correlated to grain boundary energies and particle pinning.
- 3. The stability of Cr₂Nb, recovery, and recrystallization of Cu-FCC grain and the role of initial microstructure was evaluated with high-temperature in-situ X-ray diffraction and compared with measurements from powders. Reduced levels, in comparison to the expected value of ~ 12 wt pct based on the nominal composition, of Cr₂Nb were detected in the gas-atomized powder and as-built L-PBF samples. This discrepancy is attributed, in part, to broadening of Cu-FCC peak with locked in micro-strains in the Cu-FCC lattices. On heating to a temperature above the recrystallization temperature of Cu-FCC matrix, the diffraction peaks from Cr₂Nb strengthened. A small amount of BCC Nb was present in the powders and was not observed in the as-built or after hot isostatic pressing.

ACKNOWLEDGMENTS

The authors would like to acknowledge the Manufacturing and Materials Joining Innovation Center (Ma²JIC), made possible through awards NSF IIP-1540000 (Phase I) and NSF IIP-1822186 (Phase II) from the National Science Foundation Industry University Cooperative Research Center program (IUCRC). RPM also acknowledges the financial support of Oak Ridge National Laboratory's Graduate Opportunities (GO!) Program. A portion of this research used resources at the High Flux Isotope Reactor, a DOE Office of Science User Facility operated by the Oak Ridge National Laboratory. This paper describes objective technical results and analysis. Any subjective views or opinions that might be expressed in the paper do not necessarily represent the views of the National Aeronautics and Space Administration (NASA) or the United States Government. M. Haines and S. S. Babu's contribution to this research is

partially supported by the US Department of the Navy Office of Naval Research under ONR award number N00014-18-1-2794. Any opinions, findings, and conclusions or recommendations expressed in this material are those of the author(s) and do not necessarily reflect the views of the Office of Naval Research.

CONFLICT OF INTEREST

On behalf of all authors, the corresponding author states that there is no conflict of interest.

REFERENCES

- Ellis DL: GRCop-84: a high temperature copper alloy for highheat-flux applications, NASA/TM-2005-213566, (2005), https://nt rs.nasa.gov/citations/20050123582.
- P.R. Gradl, C.S. Protz, K. Cooper, D. Ellis, L.J. Evans, and C. Garcia: In AIAA Propulsion and Energy 2019 Forum, 2019, p 4228.
- 3. B. Blakey-Milner, P. Gradl, G. Snedden, M. Brooks, J. Pitot, E. Lopez, M. Leary, F. Berto, and A.D. Plessis: *Mater. Des.*, 2021, vol. 209, 110008.
- 4. P.R. Gradl, C.S. Protz, K. Zagorski, V. Doshi, and H. McCallum: In *AIAA Propulsion and Energy 2019 Forum*, 2019, p 4390.
- P.R. Gradl, C. Protz, S.E. Greene, D. Ellis, B. Lerch, and I. Locci: In 53rd AIAA/SAE/ASEE Joint Propulsion Conference, 2017, p 4670
- F. Kerstens, A. Cervone, and P. Gradl: *Acta Astronaut.*, 2021, vol. 182, pp. 454–65.
- A.H. Seltzman and S.J. Wukitch: Fusion Eng. Des., 2020, vol. 159, 111726.
- 8. D.L. Ellis and G.M. Michal: Precipitation strengthened high strength, high conductivity Cu-Cr-Nb alloys produced by chill block melt spinning. Final Report Ph.D. Thesis, Case Western Reserve University, 1989, https://ntrs.nasa.gov/citations/19900002537.
- D.L. Ellis, G.M. Michal GM, and N.W. Orth: Production and processing of Cu-Cr-Nb alloys. NASA-TM-102495, 1990, https:// ntrs.nasa.gov/citations/19900006737.
- D.L. Ellis and K. Hastings: Effects of Hydrogen on GRCop-84. NASA/TM-2006-214269, 2006, https://ntrs.nasa.gov/api/citations/20060017836/downloads/20060017836.pdf.
- R.P. Minneci, E.A. Lass, J.R. Bunn, H. Choo, and C.J. Rawn: *Int. Mater. Rev.*, 2021, vol. 66, pp. 394–425.
- 12. B. Dutta, S. Babu, and Bradley H Jared: Science, technology and applications of metals in additive manufacturing. Elsevier, 2019.
- P.R. Gradl, S.E. Greene, C. Protz, B. Bullard, J. Buzzell, C. Garcia, J. Wood, R. Osborne, J. Hulka, and K.G. Cooper: In 2018 Joint Propulsion Conference, 2018, p 4625.
- P.R. Gradl, C.S. Protz, D.L. Ellis, and S.E. Greene: Progress in additively manufactured copper-alloy GRCop-84, GRCop-42, and bimettalic combustion chambers for liquid rocket engines. In *Proceedings of 70th International Astronautical Congress*; 2019 Oct 21–25, Washington, D.C, 2019, https://ntrs.nasa.gov/citations/20190033311.
- 15. C. Hayes, E. Brown, and B. Kappes: In 2018 Joint Propulsion Conference, 2018, p 4624.
- 16. A.H. Seltzman and S.J. Wukitch: Fusion Sci. Technol., 2021, vol. 77, pp. 641–46.
- 17. G. Demeneghi, B. Barnes, P. Gradl, J.R. Mayeur, and K. Hazeli: *Mater. Sci. Eng. A*, 2021, vol. 820, p. 141511.
- 18. Paulo Rangel Rios and Dana Zöllner: *Mater. Sci. Technol.*, 2018, vol. 34, pp. 629–38.
- 19. J.N. DuPont: ASM Handbook 6a 2011, pp. 96-114.
- 20. S. Das, D.L. Bourell, and S.S. Babu: *Mrs Bull.*, 2016, vol. 41, pp. 729–41.
- S.A. David and J.M. Vitek: *Int. Mater. Rev.*, 1989, vol. 34, pp. 213–45.

- X. Zhang, C.J. Yocom, B. Mao, and Y. Liao: *J. Laser Appl.*, 2019, vol. 31, p. 31201.
- F. Yan, W. Xiong, and E.J. Faierson: *Materials*, 2017, vol. 10, p. 1260.
- 24. S. Das: Adv. Eng. Mater., 2003, vol. 5, pp. 701–11.
- 25. W.J. Sames, F.A. List, S. Pannala, R.R. Dehoff, and S. Suresh Babu: *Int. Mater. Rev.*, 2016, vol. 61, pp. 315–60.
- 26. F. Bachmann, R. Hielscher, and H. Schaeben: Solid State Phenom., 2010, vol. 160, pp. 63-68.
- G.J. Butterworth and C.B.A. Forty: *J. Nucl. Mater.*, 1992, vol. 189, pp. 237–76.
- A. Plotkowski, J. Ferguson, B. Stump, W. Halsey, V. Paquit, C. Joslin, S.S. Babu, A.M. Rossy, M.M. Kirka, and R.R. Dehoff: *Addit. Manuf.*, 2021, vol. 46, p. 102092.
- D. Rosenthal: Trans. Am. Soc. Mech. Eng., 1946, vol. 68, pp. 849–65.
- 30. D. Rosenthal: Weld. J., 1941, vol. 20, pp. 220s-s234.
- 31. Øystein Grong: (No Title) 1997.
- 32. M. Haines, A. Plotkowski, C.L. Frederick, E.J. Schwalbach, and S.S. Babu: *Comput. Mater. Sci.*, 2018, vol. 155, pp. 340–49.
- 33. B.H. Toby: *J. Appl. Crystallogr.*, 2001, vol. 34, pp. 210–13.
- 34. B.H. Toby and R.B. Von Dreele: *J. Appl. Crystallogr.*, 2013, vol. 46, pp. 544–49.
- 35. R.B. Von Dreele and A.C. Larson: *Los Alamos Natl. Lab. Rep. LAUR*, 2004, vol. 748, pp. 86–748.
- 36. M. Venkatraman and J.P. Neumann: *Bull. Alloy Phase Diagr.*, 1986, vol. 7, pp. 462–66.
- 37. P. Nandwana, W.H. Peter, R.R. Dehoff, L.E. Lowe, and M.M. Kirka: *Metall. Mater. Trans. B*, 2016, vol. 47, pp. 754–62.
- 38. V. Juechter, T. Scharowsky, R.F. Singer, and C. Körner: *Acta Mater.*, 2014, vol. 76, pp. 252–58.
- S.J. Foster, K. Carver, R.B. Dinwiddie, F. List, K.A. Unocic, A. Chaudhary, and S.S. Babu: *Metall. Mater. Trans. A*, 2018, vol. 49, pp. 5775–98.
- 40. J.A. Dantzig and M. Rappaz: Solidification: -Revised & Expanded, EPFL Press, Lausanne, 2016.
- 41. M. Rappaz, S.A. David, J.M. Vitek, and L.A. Boatner: *Metall. Trans. A*, 1990, vol. 21, pp. 1767–82.
- 42. S.A. David, S.S. Babu, and J.M. Vitek: *Jom*, 2003, vol. 55, pp. 14–20.
- 43. J.C. Villafuerte, H.W. Kerr, and S.A. David: *Mater. Sci. Eng. A*, 1995, vol. 194, pp. 187–91.

- 44. M. Maalekian, H. Azizi-Alizamini, and M. Militzer: *Metall. Mater. Trans. A*, 2016, vol. 47A, pp. 608–22.
- 45. Ge. Wang, H. Ouyang, C. Fan, Q. Guo, Z. Li, W. Yan, and Z. Li: *Mater. Res. Lett.*, 2020, vol. 8, pp. 283–90.
- R. Viswanathan and C.L. Bauer: Acta Metall., 1973, vol. 21, pp. 1099–1109.
- 47. R.A. Vandermeer, D. Juul Jensen, and E. Woldt: *Metall. Mater. Trans. A*, 1997, vol. 28A, pp. 749–54.
- 48. M.A. Tschopp and D.L. McDowell: *Philos. Mag.*, 2007, vol. 87, pp. 3871–92.
- J.R. Porter and F.J. Humphreys: Met. Sci., 1979, vol. 13, pp. 83–88
- F.J. Humphreys and M.G. Ardakani: *Acta Mater.*, 1996, vol. 44, pp. 2717–27.
- 51. T. Watanabe: J. Phys. Coll., 1988, vol. 49, pp. C5-507-5-519.
- J. Raplee, J. Gockel, F. List III., K. Carver, S. Foster, T. McFalls,
 V. Paquit, R. Rao, D.W. Gandy, and S.S. Babu: Sci. Technol. Weld. Joining, 2020, vol. 25, pp. 679–89.
- Ellis, D.L., Misra, A.K. and Dreshfield, R.L., 1994. Effect of Hydrogen Exposure on a Cu-8 Cr-4 Nb Alloy for Rocket Motor Applications. Hydrogen Effects in Materials (No. NASA-TM-106429).
- B.D. Cullity and S.R. Stock: Elements of X-ray Diffraction, 3rd ed. Prentice Hall, Upper Saddle River, NJ, 2001.
- 55. A.R. Denton and N.W. Ashcroft: *Phys. Rev.A*, 1991, vol. 43, p. 3161
- K. Hono and S. S. Babu: In *Physical Metallurgy (Fifth Edition)*,
 ed. David E. Laughlin and Hono Kazuhiro Elsevier: Oxford, 2014,
 pp 1453–1589.
- T.F. Kelly and M. Miller: Rev. Sci. Instrum., 2007, vol. 78, p. 031101.
- 58. David L Ellis, Dennis J Keller, and Michael Nathal: 2000.

Publisher's Note Springer Nature remains neutral with regard to jurisdictional claims in published maps and institutional affiliations.

Springer Nature or its licensor (e.g. a society or other partner) holds exclusive rights to this article under a publishing agreement with the author(s) or other rightsholder(s); author self-archiving of the accepted manuscript version of this article is solely governed by the terms of such publishing agreement and applicable law.